Deep-Sea Research II 116 (2015) 303–320

Contents lists available at ScienceDirect

Deep-Sea Research II

journal homepage: www.elsevier.com/locate/dsr2

Size-fractionated major particle composition and concentrations from the US GEOTRACES North Atlantic Zonal Transect

Phoebe J. Lam [a,*], Daniel C. Ohnemus [b,1], Maureen E. Auro [a]

[a] Department of Marine Chemistry and Geochemistry, Woods Hole Oceanographic Institution, Woods Hole, MA 02543, USA
[b] MIT-WHOI Joint Program in Oceanography, Massachusetts Institute of Technology/Woods Hole Oceanographic Institution, Woods Hole, MA 02543, USA

ARTICLE INFO

Available online 18 November 2014

Keywords:
Particles
SPM
$CaCO_3$
Opal
Biogenic silica
POC
Ballast
Dust
Lithogenic material

ABSTRACT

The concentration and the major phase composition (particulate organic matter, $CaCO_3$, opal, lithogenic matter, and iron and manganese oxyhydroxides) of marine particles is thought to determine the scavenging removal of particle-reactive TEIs. Particles are also the vector for transferring carbon from the atmosphere to the deep ocean via the biological carbon pump, and their composition may determine the efficiency and strength of this transfer. Here, we present the first full ocean depth section of size-fractionated (1–51 μm, > 51 μm) suspended particulate matter (SPM) concentration and major phase composition from the US GEOTRACES North Atlantic Zonal Transect between Woods Hole, MA and Lisbon, Portugal conducted in 2010 and 2011. Several major particle features are notable in the section: intense benthic nepheloid layers were observed in the western North American margin with concentrations of SPM of up to 1648 μg/L, two to three orders of magnitude higher than surrounding waters, that were dominated by lithogenic material. A more moderate benthic nepheloid layer was also observed in the eastern Mauritanian margin (44 μg/L) that had a lower lithogenic content and, notably, significant concentrations of iron and manganese oxyhydroxides (2.5% each). An intermediate nepheloid layer reaching 102 μg/L, an order of magnitude above surrounding waters, was observed associated with the Mediterranean Outflow. Finally, there was a factor of two enhancement in SPM at the TAG hydrothermal plume due almost entirely to the addition of iron oxyhydroxides from the hydrothermal vent. We observe correlations between POC and $CaCO_3$ in large (> 51 μm) particles in the upper 2000 m, but not deeper than 2000 m, and no correlations between POC and $CaCO_3$ at any depth in small (< 51 μm) particles. There were also no correlations between POC and lithogenic material in large particles. Overall, there were very large uncertainties associated with all regression coefficients for mineral ballast ("carrying coefficients"), suggesting that mineral ballast was not a strong predictor for POC in this section.

1. Introduction

Particles in the ocean, or suspended particulate matter (SPM), play a vital role in the cycling of trace elements and isotopes (TEIs), and are thus a key parameter in the international GEOTRACES program (GEOTRACES, 2006). Particles can be delivered by sources external to the ocean and bring TEIs to the water column. Particles can also be generated within the ocean through biological carbon fixation and biogenic and abiotic mineral precipitation, and thus participate in internal cycling of TEIs. Both externally and internally derived particles participate in the removal of TEIs from the water column through scavenging of dissolved TEIs, sinking, and burial in sediments (Jeandel et al., in press).

SPM in the ocean generally comprises three major biogenic phases: particulate organic matter (POM) and the biogenic minerals calcium carbonate ($CaCO_3$) and biogenic silica (BSi, also known as opal) (Bishop et al., 1977). In some ocean basins and near continental margins, abiotic components such as lithogenic material from atmospheric dust deposition or sediment resuspension and transport are also important. There are many more components that contribute to SPM, but they are rarely a significant fraction of the total SPM mass. In special circumstances such as near hydrothermal vents or sediments, oxyhydroxides of Fe and/or Mn can also be important (German and Von Damm, 2003; Macdonald and Gobeil, 2012).

Both particle concentration and composition affect scavenging of dissolved TEIs. Elevated particle concentrations provide more surfaces for scavenging, while different particle compositions may affect

* Corresponding author. Now at Department of Ocean Sciences, University of California, Santa Cruz, Santa Cruz, CA 95064, USA.
E-mail address: pjlam@ucsc.edu (P.J. Lam).
[1] Bigelow Laboratory for Ocean Sciences East Boothbay, ME 04544, USA.

http://dx.doi.org/10.1016/j.dsr2.2014.11.020

the particle affinity of a TEI. The role of SPM composition in TEI scavenging has been studied for the naturally occurring, strongly particle-reactive thorium isotopes (^{234}Th, ^{228}Th, and ^{230}Th), but there is not yet consensus over which phase exerts the most influence in scavenging. It has been variously proposed that the scavenging efficiency of ^{230}Th is controlled by $CaCO_3$ (Chase et al., 2002, 2003), lithogenic material (Luo and Ku, 2004; Roy-Barman et al., 2009), and/or Mn oxyhydroxides (Roy-Barman et al., 2005). All of these studies were conducted on sinking particles collected by sediment traps, where the identification of a single controlling factor can be confounded by fortuitous correlations between multiple factors (e.g., $CaCO_3$ and MnO_2 Roy-Barman et al., 2005), and may help explain the contradictory conclusions reached by various studies (Jeandel et al., in press; Roy-Barman et al., 2005). Indeed, most scavenging likely occurs onto small, suspended particles, which are more abundant, have more available surface area, and have a longer residence time in the water column than sinking particles. The particle dynamics that connect small, suspended particles onto which most scavenging occurs, to the large, sinking particles collected by sediment traps vary between different ecosystem types, potentially complicating the interpretation of sediment trap material.

Focusing on suspended particles allows a more direct study of the effect of particle composition on scavenging, without the complications of particle dynamics. Indeed, scavenging of particle-reactive TEIs has been studied on suspended particles collected by in-situ filtration (e.g., Bacon and Anderson, 1982), but not yet with the additional information provided by major particle composition. The addition of a sinking particle size class, either using size-fractionation during in-situ pumping, or pairing pumped samples (suspended particles) with sediment trap samples (sinking particles), additionally allows the study of particle dynamics that connect suspended and sinking particles through particle aggregation, disaggregation, and sinking (Cochran et al., 2000; Marchal and Lam, 2012; Murnane et al., 1994; Nozaki et al., 1987; Ohnemus and Lam, 2015). The relatively large volumes filtered (hundreds to thousands of liters) using in-situ filtration allows the measurement of many analytes on subsamples from the same filter, including various particle-reactive TEIs and all the major and minor phases of SPM, provided that care is taken to ensure even distribution of particles during sampling and processing (Bishop et al., 2012).

In addition to the effect of particle composition on scavenging, the mineral phases of SPM (i.e., $CaCO_3$, opal, and lithogenic material) may help ballast POC to depth (Armstrong et al., 2002). Strong correlations are observed between POC and $CaCO_3$ flux in deep (>2000 m) sediment traps (François et al., 2002; Klaas and Archer, 2002), but similar correlations are typically not observed between shallow POC and $CaCO_3$ export flux at the base of the euphotic zone (Le Moigne et al., 2012). An increasing number of studies suggest that the observed ballast mineral correlations reflect underlying ecosystem control of POC flux to depth, for which the ballast minerals are simply proxies (Henson et al., 2012; Lam et al., 2011; Wilson et al., 2012). Further, studies have indicated regionally specific carrying coefficients of ballast minerals for POC (i.e., the regression coefficients for a multiple linear regression of POC flux as a function of $CaCO_3$, opal, and lithogenic material) (Ragueneau et al., 2006; Wilson et al., 2012).

Here, we present the concentrations and major phase compositions of SPM in two size fractions (1–51 μm and >51 μm) collected by in-situ filtration during the U.S. GEOTRACES North Atlantic Zonal Transect. The data presented here should be of use for investigating the effect of particle concentration and composition on the scavenging of particle-reactive TEIs, as well as allow examination of POC—ballast mineral correlations in the North Atlantic.

2. Methods

2.1. Cruise track and hydrography

The US GEOTRACES North Atlantic Zonal Transect was completed in two stages on the *R/V Knorr*: KN199-4 (hereafter "GT10") departed from Lisbon, Portugal and ended in Cape Verde in October-November 2010 and sampled stations GT10-1 through GT10-12; KN204-1 (hereafter "GT11") departed from Woods Hole, MA and ended in Cape Verde in October-December 2011 and sampled stations GT11-1 through GT11-24 (Fig. 1). Full ocean depth profiles of size-fractionated particles were collected by in-situ pumping at 8 stations on GT10 and 14 stations on GT11. Typical profiles were 16-depth resolution, with 8 depths in the upper 1000 m, and 8 depths between 1000 m and the ocean bottom. Pumps were programmed for 4 h of pumping, which resulted in a median of 461 L filtered through the Supor filter, and 1167 L filtered through the QMA filter.

The meridional component of the cruise track (GT10-1 to GT10-8), from Lisbon to the Mauritanian coast, is characterized by North Atlantic Central Water (i.e., relatively warm and salty waters between 20–30°W and 30–35°N that characterize the North Atlantic subtropical thermocline) in the upper 500 m, high salinity Mediterranean Outflow Waters between 500 and 1500 m, and North Atlantic Deep Water with some Antarctic Bottom Water

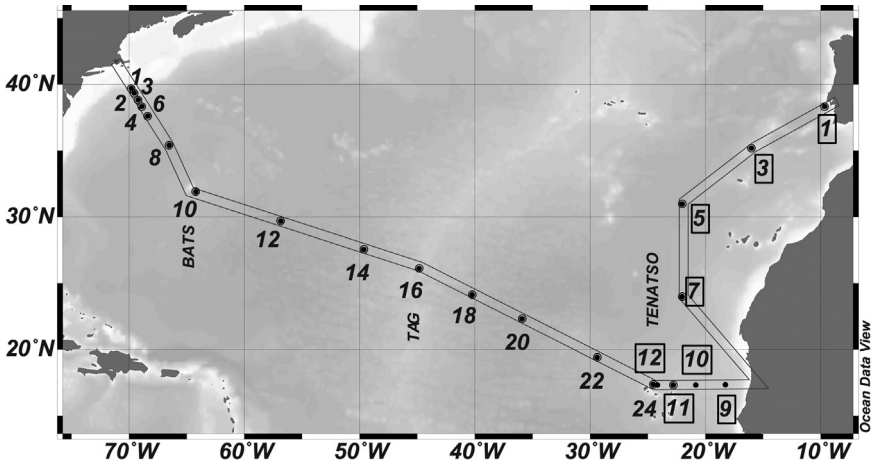

Fig. 1. Map of stations and section definition for US GEOTRACES North Atlantic Zonal Transect. Numerical annotations are station numbers for the GT10 and GT11 cruises. Station numbers from the first cruise, GT10, are boxed.

below that (Jenkins et al., 2015). The zonal part of the transect can be separated into three sections. From west to east, these are: the line W section between Woods Hole, MA and Bermuda (stations GT11-1 to GT11-10), the oligotrophic open ocean section between Bermuda and Cape Verde Islands (stations GT11-10 to GT11-24), and the Mauritanian Upwelling section between Cape Verde and the Mauritanian coast (GT10-12 to GT10-9). North Atlantic Central Water dominates the thermocline (upper ~600 m) in the line W and oligotrophic sections, whereas Atlantic Equatorial Water (i.e., fresher and cooler thermocline waters at 20–40°W, 5–10°N) is more important in the thermocline of the Mauritanian Upwelling part of the section (Jenkins et al., 2015). Northern-sourced Upper and Central Labrador Seawater are the dominant intermediate water masses along line W, whereas southern-sourced Antarctic Intermediate Water and Upper Circumpolar Deep Water dominate in the Mauritanian upwelling section, with a mixture of northern- and southern-sourced intermediate waters in the oligotrophic section. A similar pattern of more northern-sourced waters in the west and more southern-sourced waters in the east characterizes the deep waters of the zonal section (Jenkins et al., 2015).

2.2. Particle sampling

Size-fractionated particles were collected using McLane Research in-situ pumps (WTS-LV) that had been modified to accommodate two flowpaths (Cutter et al., 2010; Lam and Morris, Patent pending). Typically, two casts of 8 pumps each and two filter holders per pump were deployed to collect a 16-depth profile. The wire-out was used to target nominal depths during deployment. A self-recording Seabird 19plus CTD was deployed at the end of the line for all casts and used to correct for wire angle to determine actual depth. On the second cruise, a 12 kHz pinger was attached to the Seabird CTD, and three RBR pressure loggers were also attached to pumps #2, #5, and #8 to further correct for actual depths during pumping. More details on pump sampling are described in Ohnemus and Lam, 2015.

Filter holders used were 142 mm-diameter "mini-MULVFS" style filter holders with two stages for two size fractions and multiple baffle systems designed to ensure even particle distribution and prevent particle loss (Bishop et al., 2012). One filter holder/flowpath was loaded with a 51 μm polyester mesh prefilter (Sefar 07-51/33) followed by paired quartz fiber filters (Whatman QMA). The other filter holder/flowpath was also loaded with a 51 μm prefilter, but followed by paired 0.8 μm polyethersulfone (Pall Supor800) filters. The 51 μm prefilters and QMA filters were underlain with 150 μm polyester mesh support filters (Sefar 07-150/41) that were not analyzed, but facilitated sample handling. Since both the Supor and QMA filters are depth filters, deploying them as pairs (one filter stacked on top of another) increases the efficiency of particle capture if both filters are analyzed. These filter combinations were chosen as the best compromise after extensive testing during the intercalibration process (Bishop et al., 2012). Because of resource constraints, however, we only analyzed the top filter. Each cast also had a full set of "dipped blank" filters deployed. These were the full filter sets (prefilter followed by paired QMA or paired Supor filters) sandwiched in a 1 μm polyester mesh filter, loaded into perforated polypropylene containers, and attached with plastic cable ties to a pump frame, and deployed. Dipped blank filters were exposed to seawater for the length of the deployment and processed and analyzed as regular samples, and thus functioned as full seawater process blanks.

All filters and filter holders were acid leached prior to use according to methods recommended in the GEOTRACES sample and sample-handling Protocols (GEOTRACES, 2010). QMA filters were additionally combusted at 450 °C for 4 h.

Upon recovery, excess seawater in the filter holder headspace was immediately sucked down on deck and filter holders carried into a HEPA-filtered environment. Particles from the Supor-side 51 μm prefilter were rinsed using 0.2 μm filtered seawater onto a 25 mm silver membrane filter (1.2 μm; Sterlitech) and dried at 50 °C for later analysis of >51 μm POC. QMA filters were also dried at 50 °C for later analysis of 1–51 μm POC. A one-eighth subsample of the QMA-side >51 μm prefilter was rinsed using 0.2 μm filtered seawater from the trace-metal clean fish onto a 25 mm 0.8 μm polyethersulfone (Pall Supor800) filter for later total digests for determination of >51 μm lithogenic material from Al and Ti. The remaining QMA-side 51 μm prefilter and Supor filters were lightly misted with ultrapure water under vacuum, and dried in a laminar flow bench. Subsamples of the dried QMA prefilter were analyzed for >51 μm $CaCO_3$ and biogenic silica (opal). Subsamples of the dried Supor filters were analyzed for 1–51 μm $CaCO_3$, biogenic Si, and lithogenic material.

Throughout this paper, the 1–51 μm and >51 μm size fractions will be referred to as SSF (small size fraction) and LSF (large size fraction), respectively, and the total (>0.8 μm) is the sum of the two size fractions. All data are available on BCO-DMO at www.bco-dmo.org/dataset/3871.

2.3. Particle composition

2.3.1. Particulate inorganic carbon

Particulate inorganic carbon (PIC) was measured either directly by coulometry (Honjo et al., 1995) on two 12 mm QMA punches (2% of filter area for the SSF) or a 1/16 polyester prefilter for the LSF, or as $CaCO_3$ from the measurement of salt-corrected Ca (using Na for salt correction) (Lam and Bishop, 2007) on two 12mm QMA punches (SSF), or 1/16 subsamples of Supor or polyester prefilter (LSF). Salt-corrected Ca was measured three ways: (1) by ICP–MS at WHOI following a 2 h room temperature 25% glacial acetic acid leach, which was dried down and brought back up in 5% HNO_3; (2) by ICP–MS at WHOI following a 5% (0.6 N) HCl leach for 12–16 h at 60 °C and diluted to 1% HCl; and (3) by ICP–AES at Boston University following a 5% HCl leach overnight at room temperature. Intercomparability between methods was tested by running select samples in replicate by different methods. PIC methods by coulometry and by ICP–MS had good intercomparability. There was a 20–30% offset in samples on Supor filters and polyester prefilters analyzed by ICP–AES compared to the other methods. These data from ICP–AES were normalized using replicate analyses from a depth profile (GT11-8 for Supor samples; GT11-24 for prefilter samples). The resulting dataset has improved oceanographic consistency. QMA punches analyzed by ICP–AES, however, were significantly higher than the rest of the cruise. This filter type was used to determine SSF PIC at most of the meridional stations (GT10-3, 5, 7) and the deep cast (>1000 m) of GT10-1. The dipped blanks for these samples were highly variable, and several replications with Supor filters were poor. Further, the fraction of total particulate carbon (TPC) that was PIC at these stations was anomalously high (mean PIC:TPC below 250 m was 0.59 ± 0.31 compared to 0.19 ± 0.10 for the oligotrophic section of the zonal transect). We hypothesize that these samples had problems with poorly constrained salt corrections. Because a reasonable oceanographic explanation could not be found to explain these anomalies in SSF PIC, and given the different methodology and high variability in blanks and replicates, we conclude that the PIC data for these samples are not trustworthy. Because PIC is an essential component of calculating suspended particulate mass (SPM—Section 2.3.6), we estimate PIC for these stations by multiplying the mean PIC:TPC determined in the upper 250 m (0.07 ± 0.04) and below 250 m (0.19 ± 0.10) of the oligotrophic section of the

zonal transect by the measured TPC in the meridional transect. This assumes that the similar hydrographies of these two sections should result in similar PIC:TPC. Because GT10-1 is strongly influenced by particles from the Mediterranean Outflow and is thus different than the oligotrophic mean, we multiplied TPC in the deep cast of GT10-1 by the mean PIC:TPC in the 250–1000 m range from that station measured by coulometry (0.30 ± 0.09). For the purposes of the ballast correlations (Section 4.2), we excluded meridional SSF PIC samples from consideration.

When available, the reported error in the full dataset (archived at BCO–DMO) is the standard deviation of replicate analyses (after normalization); if no replicate analyses were made, the reported error is the standard deviation of the dipped blank filters used in the blank subtraction for each method and filter type, adjusted for volume filtered. For the meridional stations, the error is propagated from the standard deviation of the mean PIC:TPC ratios used to estimate PIC and the error of the TPC measurement (see Section 2.3.2). The standard deviations of the blank subtractions varied from 3 to 61 μg/filter, depending on filter type and method, resulting in typical relative errors of 0.4 to 18% for the samples (Table 1). The mass of $CaCO_3$ was calculated stoichiometrically from the mass of PIC ($CaCO_3$ [μg/L]= 100.08 g $CaCO_3$/12 g C × PIC [μg/L]).

2.3.2. Particulate organic matter (POM)

Total particulate carbon (TPC) was measured using a Flash EA1112 Carbon/Nitrogen Analyzer using a Dynamic Flash Combustion technique at the WHOI Nutrient Analytical Facility. Suspended particles (1–51 μm) were measured for total particulate carbon using one or two 12 mm-diameter punches from the top QMA filter, representing the equivalent of 10–20 L of material. For the >51 μm size fraction, particles from half or a whole 51 μm polyester prefilter were rinsed at sea with 1 μm-filtered seawater onto a 25 mm 0.8 μm Sterlitech Ag filter or 25 mm pre-combusted Whatman QMA filter before being dried at 60 °C. A quarter of the Ag or QMA filter containing rinsed particles was analyzed for total particulate carbon, typically representing 60–120 L of material.

The standard deviation of the dipped blank filters was used in the blank subtraction to estimate error in the TPC measurement. For TPC in the suspended (1–51 μm) size fraction (TPC_SSF), the standard deviation of 8 dipped blank or failed pump (pumps that never turned on, or that shut off after <5% of programmed water volume was filtered) QMA filters was 83 μg C per 142 mm QMA filter, resulting in a typical relative error of 2% (Table 1). For TPC in the sinking (>51 μm) size fraction, the standard deviations of 8 dipped blank prefilters rinsed onto Ag and onto QMA were 6.2 μg C per 142 mm prefilter and 7.1 μg C per 142 mm prefilter, respectively, resulting in typical relative errors of 1% (Table 1).

POC is calculated as the difference between TPC and PIC. Any negative numbers were set to 0. Errors were propagated from the values used for TPC and PIC and were typically 7–8% (Table 1). POM is calculated from POC using a weight ratio of 1.88 g POM/g POC (Lam et al., 2011).

2.3.3. Biogenic silica (bSi)

A 1/16 subsample of the top 0.8 μm Supor filter, equivalent to ~30 L, or of the 51 μm polyester prefilter above the QMA filter, equivalent to ~60 L, was analyzed for amorphous/biogenic Si concentrations using standard spectrophotometric detection of the blue silico-molydate complex (Parsons et al., 1984). We slightly modified the time-series approach developed for marine sediments to correct for the contribution of lithogenic silica to the leachate (DeMaster, 1981), using 20 mL 0.2 M NaOH at 85 °C for the leach, and taking a 1.6 mL subsample every hour for 3 h. The slope of the fit was negligible for shallow samples but generally increased with depth of the sample, a reflection of the increasing importance of lithogenic silica to total silica with depth; we thus proceeded with a 1 h incubation time for shallow cast samples (<900 m), and continued the time-series approach for deep cast samples (>900 m). Dipped blank filters from both shallow and deep casts were used to correct the Supor filter data. For >51 μm samples on polyester prefilters, blank corrections were made using the average failed pump values because of anomalously high prefilter dipped blank values.

The standard deviation of the dipped blank filters was used in the blank subtraction to estimate error in the reported opal value,

Table 1
Standard deviations of the dipped blanks for major particle phases used to estimate errors in the measurements. Typical (mean), maximum, and minimum relative errors for the range in sample loadings that these represent are indicated.

Method	Size fraction: filter type	Blank Std Dev (μg/filter)	Typical (%)	Max (%)	Min (%)
Particulate inorganic carbon (PIC)					
Coulometry	1–51 μm: QMA	18	2.0	4.4	1.2
	>51 μm: Prefilter	18	2.6	8.4	0.8
ICP–MS	0.8–51 μm: Supor	11	3.3	41.1	0.1
	>51 μm: Prefilter	3	0.4	3.6	0.0
ICP–AES	0.8–51 μm: Supor-run1	61	18.0	274.0	2.6
	0.8–51 μm: Supor-run2	12	11.0	66.0	3.5
	>51 μm: Prefilter	7	1.3	37.6	0.2
Total particulate carbon (TPC)					
Combustion	1–51 μm: QMA	83	2.1	36.2	0.3
	>51 μm: Prefilter onto Ag	7.1	1.3	37.6	0.2
	>51 μm: Prefilter onto QMA	6.2	1.2	4.9	0.3
Biogenic Silica (BSi)					
1 h Incubation	0.8–51 μm: Shallow Supor	6	1.9	195.0	0.4
Time-series	0.8–51 μm: Deep Supor	4	1.6	275.0	0.1
1 h incubation	>51 μm: Shallow Prefilter	24	3.1	78.0	0.2
Time-series	>51 μm: Deep Prefilter	8	4.8	2250	0.5
Lithogenic material (Litho)					
Calculated from Al	0.8–51 μm: Supor	N/A	16.2	43.6	14.4
	>51 μm: Prefilter onto Supor	N/A	14.9	18.5	14.4
Particulate organic carbon (POC)					
Calculated from TPC and PIC	<51 μm	N/A	8.2	98.4	0.7
	>51 μm	N/A	6.9	147.1	0.1
Suspended particulate matter (SPM)					
Chemical dry weight	<51 μm	N/A	8.9	36.9	1.1
	>51 μm	N/A	7.1	44.1	0.3

and ranged from 4 to 24 μg/filter, depending on method and filter type, leading to typical relative errors of 1–5% (Table 1).

The mass of biogenic silica (opal) was calculated assuming a hydrated form of silica: $SiO_2 \cdot (0.4H_2O)$ (Mortlock and Froelich, 1989): 67.2 g opal/mol bSi.

2.3.4. Lithogenic material

Total particulate Al, Ti, Mn, and Fe were determined using the "Piranha" digest method (Ohnemus et al., 2014), which completely digests the Supor filter, followed by analysis by sector field ICP–MS, and is described for these samples in Ohnemus and Lam, 2015. Al is usually used as a tracer of lithogenic material since it is the third most abundant element in Earth's crust after Si and O. Al has the added advantage that its concentration does not vary greatly between upper continental crust (UCC Al=8.04% by weight) and bulk continental crust (BCC Al=8.41 wt%) (Taylor and McLennan, 1995) values, so estimates of lithogenic mass are not very sensitive to lithogenic source regions. Al may be fairly susceptible to scavenging from dissolved sources, however, which would lead to overestimates of lithogenic mass, especially in coastal samples. Ti seems less affected by scavenging (Dammshäuser et al., 2011; Dymond et al., 1997; Murray and Leinen, 1996; Ohnemus and Lam, 2015), but has the disadvantage of varying greatly as a function of different source regions (e.g., UCC Ti=0.3 wt% and BCC Ti=0.54 wt%) (Taylor and McLennan, 1995). We thus calculate lithogenic mass two ways: (1) using the UCC Al concentration of 8.04% to calculate lithogenic mass (Litho_AlUCC), and (2) using Ti, a lithogenic tracer that appears to be less affected by scavenging (Litho_TiDust):

$$\text{Litho\_AlUCC}\,[\mu g/L] = \text{Al}\,[nM] \times 27\ g/mol/0.0804\ g\ Al/g\ UCC \quad (1)$$

$$\text{Litho\_TiDust}\,[\mu g/L] = \text{Ti}\,[nM] \times 47.9\ g/mol/0.006\ g\ Ti/g\ dust \quad (2)$$

For Ti, we make the assumption that the source of the lithogenic material is from African dust, and use the concentration of Ti and Al in aerosols collected on four samples between Cape Verde and Mauritania (Shelley and Landing, personal communication) to estimate a Ti composition of 0.6 wt% to estimate lithogenic mass (Litho_TiDust).

Using Al as a lithogenic tracer leads to higher estimates of lithogenic mass, especially at high lithogenic concentrations of the North American, Mauritanian, and Iberian margins (Fig. 2). The overall slope of the relationship between lithogenic mass determined by Al compared to Ti is 1.4, indicating that the lithogenic mass estimate would be higher by 40% if using Al. Restricting sample comparisons to those from the oligotrophic gyre, however, results in more equivalent estimates of lithogenic mass (Al:Ti slope=0.94), suggesting that the discrepancy between the two lithogenic tracers applies primarily to the margins, where lithogenic concentrations are highest. This could be due to enhanced scavenging of Al compared to Ti at the margins (cf. Dymond et al., 1997; Murray and Leinen, 1996), or to the increasing importance of different lithogenic sources at the margins. Several observations point to a North American source of lithogenic material along the western margin and an African source of lithogenic material in the eastern and central parts of the basin (Ohnemus and Lam, 2015; Revels et al., 2015). Because of this expected difference in lithogenic source, we proceed here with the Al-based estimate of lithogenic material, which is less sensitive to source variability than Ti, with the caveat that enhanced Al scavenging may make this an overestimate.

We use the mean relative standard deviation between lithogenic mass estimated by Al (Eq. (1)) and Ti (Eq. (2)) (14%) as an estimate of the uncertainty in scaling Al to lithogenic mass, and propagate this uncertainty and the analytical uncertainty in the Al measurement by ICP–MS (typically 6%). Mean relative errors for lithogenic material were 16% and 15% for SSF and LSF, respectively (Table 1).

2.3.5. Fe and Mn oxyhydroxides

Fe and Mn in oxyhydroxides were calculated by subtracting Fe and Mn associated with lithogenic material. Compared to Al, crustal Fe, Mn, and Ti vary more widely as a function of source material, but the ratios of Fe and Mn to Ti are less variable. For example, whereas absolute concentrations of Fe, Mn, and Ti are about a factor of two higher in BCC compared to UCC, the Fe/Ti and Mn/Ti mole ratios in UCC are 10.0 and 0.17, respectively, which are similar to Fe/Ti and Mn/Ti mole ratios in BCC of 11.2 and 0.23. Here, we assume that lithogenic Fe and Mn are best approximated by Saharan dust, and so use the molar ratios to Ti from aerosols collected on four samples between Cape Verde and Mauritania (Fe/Ti=8.7 and Mn/Ti=0.13) (Shelley and Landing, personal communication) to subtract the lithogenic contributions of Fe and Mn to derive $Fe(OH)_3$_TiDust and MnO_2_TiDust. We approximate the formulae for Fe and Mn oxyhydroxides to be $Fe(OH)_3$ (ferrihydrite approximation) and MnO_2 (birnessite approximation), with formula weights 106.9 g $Fe(OH)_3$/mol Fe and 86.9 g MnO_2/mol Mn, and negative numbers were set to 0. The formulae are:

$$Fe(OH)_2[\mu g/L] = (Fe[nM] - (Ti[nM] \times 8.7\ nmol\ Fe/nmol\ Ti)) \times 106.9\ ng\ Fe(OH)_3/nmolFe/1000 \quad (3)$$

$$MnO_2[\mu g/L] = (Mn[nM] - (Ti[nM] \times 0.13\ nmol\ Mn/nmol\ Ti)) \times 86.9\ ng\ MnO_2/nmol\ Mn/1000 \quad (4)$$

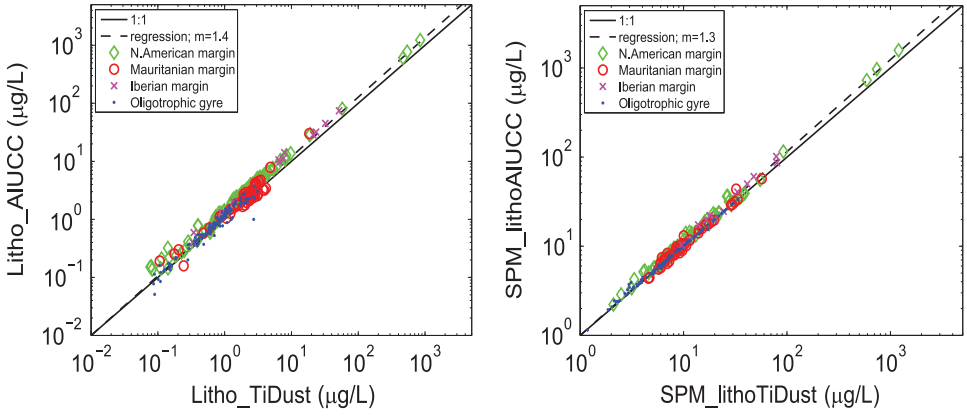

Fig. 2. Comparison of lithogenic mass estimated using Al vs. using Ti as tracers. Data are color coded by station type, where N. American margin are stations GT11-1 through 10 (green diamonds); Mauritanian margin are GT10-9 through -12 (red circles); Iberian margin is station GT10-1 (magenta *x*); and Oligotrophic gyre are stations GT11-12 through -24 and GT 10-3 through -7 (blue dots). The 1:1 line and regression line are indicated as solid and dashed lines, respectively. (For interpretation of the references to color in this figure legend, the reader is referred to the web version of this article.)

Variability in the Fe/Ti and Mn/Ti ratios in the aerosols and analytical errors for Fe, Mn, and Ti were propagated to determine the error for Fe and Mn oxyhydroxides. The variability in the Fe/Ti and Mn/Ti ratios in the aerosols was 2% and 6%, respectively. Typical analytical errors for Fe, Mn, and Ti are 3%, 3%, and 6%, respectively.

2.3.6. Suspended particulate mass

It is difficult to determine suspended particulate mass gravimetrically on depth filters such as Supors and QMAs because they retain significant seawater even after misting with distilled water under vacuum, and correctly correcting for the salt contribution to mass is difficult (cf., Bishop, 1991; Lam and Bishop, 2007). Instead we use the major particulate components to calculate a "chemical dry weight", which has been shown to be a reasonable estimate of gravimetrically determined particulate mass (Bishop et al., 1977). Suspended particulate mass in the sinking (>51 μm) and suspended (1–51 μm) size fractions was estimated as the chemical dry weight of the major particulate phases, which is the sum of POM, opal, $CaCO_3$, lithogenic material from Al (Litho_AlUCC), and Fe and Mn oxyhydroxides. The formula is:

$$\begin{aligned}\text{SPM\_lithoAlUCC} = {} & \text{CaCO}_3 + \text{opal} + \text{POM} + \text{Litho\_AlUCC} \\ & + \text{Fe(OH)}_3\text{\_TiDust} + \text{MnO}_2\text{\_TiDust}\end{aligned} \quad (5)$$

Errors were propagated from the errors in each component phase. Typical relative errors in SPM were 8.9% and 7.1% for SSF and LSF, respectively (Table 1).

3. Results

3.1. Section overview

3.1.1. Size-fractionated suspended particulate matter (SPM)

The section of SPM shows elevated concentrations in the euphotic zone across the section ($SPM_{TOT}(z<150\text{ m}) = 26.9 \pm 25.4$ μg/L; median ± 1 s.d.) (Fig. 3), comparable to the 25–50 μg/L observed in North Atlantic oligotrophic surface waters during GEOSECS (Brewer et al., 1976). The lowest concentrations of SPM_{TOT} are in the interior of the oligotrophic ocean ($SPM_{TOT}(1000\text{ m}>z>4000\text{ m}) = 3.7 \pm 1.2$ μg/L), and are flanked by elevated SPM near all the margins, where concentrations are 2–6 times higher than in the interior. These concentrations are comparable to deep oligotrophic SPM concentrations from GEOSECS (SPM < 12 μg/L) (Brewer et al., 1976) and to clear water minimum particle concentrations estimated from the LDGO nephelometer surveys (0.5–2.5 μg/L) (Biscaye and Eittreim, 1977). The SPM was especially elevated at station GT10-1 near the Iberian margin in Mediterranean Outflow waters at intermediate depths (500–1500 m), coinciding with a salinity maximum. The highest concentrations of SPM were found at benthic nepheloid layers along the western boundary between stations GT11-4 through GT11-10, reaching up to 1648 μg/L at GT11-4 at 3662 m (Table 2), 2–3 orders of magnitude higher than surrounding waters. A smaller benthic nepheloid layer (SPM_{SSF} = 44 μg/L; no SPM_{LSF} available) is also present at station GT10-9 at the Mauritanian margin. Finally, a midwater enhancement in SPM_{TOT} to 11.4 μg/L is observed at the TAG hydrothermal plume at station GT11-16 at 3300 m.

About 78% of the total particle mass is in the small size fraction (Fig. 4A). Particles were partitioned more strongly to the large size fraction in the zonal transect between Woods Hole and the Mauritanian margin (median ± 1 s.d. = 24 ± 10% in LSF) compared to the meridional transect between Lisbon and the Mauritanian margin (12 ± 8% in LSF). Note that these statistics are simple averages of all samples, and do not correct for the increased sampling density in the upper 500 m.

3.1.2. Size-fractionated composition: POM, $CaCO_3$, lithogenics, opal, Fe oxyhydroxides, Mn oxyhydroxides

3.1.2.1. Particulate organic carbon (POC). Like SPM, POC is elevated in the upper 150 m across the transect ($POC_{TOT}(z<150\text{ m}) = 0.80 \pm 0.67$ μM; median ± 1 s.d.) (Fig. 5). The interior of the oligotrophic gyre has the lowest POC concentrations (0.064 ± 0.02 μM) of the transect, almost two times lower than POC concentrations at the margins. POC_{TOT} at BATS (GT11-10) ranged from 1.0 μM at 41 m to 0.17 μM at 794 m, comparable to POC reported in the Sargasso Sea that ranged from 0.8 μM at 40 m to 0.09 μM at 724 m (Bishop and Fleisher, 1987), but lower than those reported from the November average from twenty-four years of sampling at the Bermuda Atlantic Time Series site (median ± 1 s.d. $z<100$ m: 1.9 ± 0.59 μM; $z=1000$ m: 0.79 ± 0.42 μM) (http://batsftp.bios.edu/BATS/bottle/bats_bottle.txt). We attribute the higher BATS values to the smaller nominal pore size of the GF/F filters used at BATS, and the

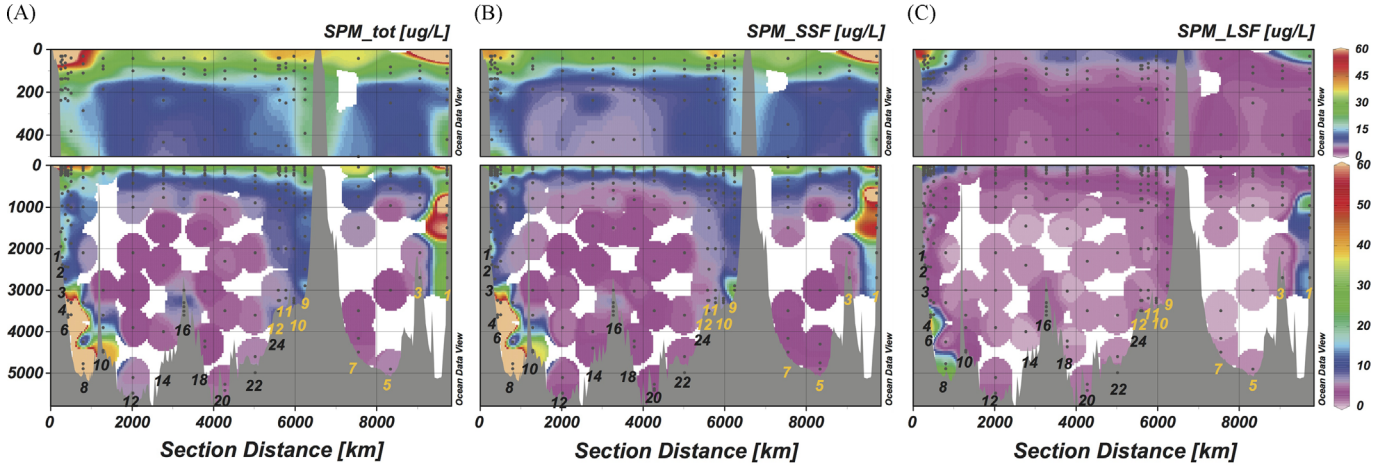

Fig. 3. Section of suspended particulate matter (SPM). (A) Total SPM (SPM_tot); (B) small size fraction (0.8–51 μm) SPM (SPM_SSF); (C) large size fraction (> 51 μm) SPM (SPM_LSF). Upper panels are the upper 500 m. Lower panels are the entire water column. All size fractions are plotted on the same colorscale. SPM_tot maxima in the benthic nepheloid layers of GT11-4 and GT11-8 are 1648 and 763 μg/L, respectively. The section starts in the west in Woods Hole, MA, crosses the basin to the coast of Africa at ~6400 km, then continues north to Lisbon, Portugal at ~9800 km. Stations sampled in 2010 on KN199-4 (USGT10) and in 2011 on KN204-1 (USGT11) are labelled in yellow and black, respectively (see Fig. 1 for map). USGT10-12 and USGT11-24 are reoccupations of the TENATSO station near Cape Verde. (For interpretation of the references to color in this figure legend, the reader is referred to the web version of this article.)

fact that the BATS POC is not corrected for DOC adsorption onto GF/F filters (Gundersen et al., 2001).

The other features of elevated SPM, namely the benthic nepheloid layers, Mediterranean Outflow, and hydrothermal plume, are also observed as elevated POC, but the enhancement of POC at these features is more modest, indicating that these features are characterized by a decrease in the relative concentrations of POC. For example, the POC_{TOT} in the benthic nepheloid layers at stations GT11-4 and -8 are enhanced by a factor of $10-40x$ versus surrounding waters, rather than by $100-1000x$ as they are for SPM; POC_{TOT} in the hydrothermal plume is enhanced by a factor of $\sim$2 to 0.12 μM compared to a factor of $\sim$3 for SPM.

Size partitioning of POC in the euphotic zone is about 76% in the small size fraction. Like for SPM, there was more LSF POC in the zonal than meridional transect (Fig. 4B). Surprisingly, the interior of the oligotrophic basin had the highest proportion of POC in the large size fraction ($38 \pm 17\%$).

3.1.2.2. Particulate inorganic carbon (PIC). Particulate inorganic carbon (PIC) is elevated in the upper 500–1000 m of the water column (Fig. 6). Mean euphotic zone PIC_{tot} concentrations in the oligotrophic zonal transect are 0.030 ± 0.016 μM, similar to the 0.01–0.075 μM range observed during the oligotrophic section of the CLIVAR A16N meridional transect (Barrett et al., 2014). The highest near-surface PIC concentrations are just off the North American (0.21 μM at GT11-1) and the Iberian (0.15 μM at GT10-1) margins at the shallowest pump depth (30 m). Although PIC typically decreases with depth due to dissolution of $CaCO_3$, Barrett et al. (2014) noted that PIC decreased particularly quickly below 400 m in the eastern tropical Atlantic (5–17 °N), coincident with a region of aragonite-undersaturated water. They also noted that biologically mediated dissolution of $CaCO_3$ from intense remineralization processes in the OMZ may have contributed to the low PIC. Our full water column data also show evidence of a small relative deficit in PIC_{SSF} in the Mauritanian Upwelling section (GT10-9 to GT10-12) centered around 1000 m (Fig. 6). Because this feature is deeper than the oxygen minimum centered around 500 m, the local deficit of PIC is more likely a result of the low saturation state of this AAIW-influenced water mass (Chung et al., 2003; Jenkins et al., 2015) rather than biologically mediated dissolution.

As with the other components, PIC is elevated at the benthic nepheloid layers on the western and eastern margins and in the Mediterranean Outflow, but it is not elevated at the hydrothermal plume. Size partitioning of PIC is about 79% in the small size fraction (Fig. 4).

3.1.2.3. Biogenic silica (BSi). Biogenic silica is elevated in the euphotic zone where it is produced, but the horizontal contrast between margin and open ocean concentrations is more striking than for other biogenic particle components (Fig. 7). BSi was exceedingly low in the oligotrophic gyre and ocean interior, with median euphotic zone concentrations between GT11-12 and GT11-22 of 5.6 ± 0.8 nM and deep (>1000 m) concentrations of 1.2 ± 0.6 nM. Euphotic zone concentrations at BATS (station GT11-10) were 37 nM, higher than typical autumn BSi concentrations measured between 1988 and 1992 (<15 nM), but well within the annual range (up to 585 nM) (Brzezinski and Nelson, 1995). BSi concentrations at BATS decreased quickly to 5 nM at 235 m, consistent with previous observations (<10 nM) (Brzezinski and Nelson, 1995). Near-margin concentrations were considerably higher, reaching a maximum in the euphotic zone of 230 nM at GT11-2 in the western margin, but only 47 nM at GT10-9 in the eastern Mauritanian margin. This part of the northwest African coast (12–20°N) experiences seasonal rather than year-round upwelling. The time of our sampling (October–November) preceded the upwelling season, which runs typically from December through May (Santos et al., 2005), explaining the low

Table 2
Characteristics of benthic nepheloid layers (BNLs) sampled by in-situ filtration.

Station	Bottom depth (m)	Max SPM_tot (μg/L)	Depth above bottom of observed Max SPM_tot (m)	Approx. thickness of BNL (m)	Integrated SPM_tot (μg/cm^2)
GT11-4	3790	1648	128	250	27773
GT11-8	4928	763	39	300	4653
GT11-10	4520	40	73	1100	2905
GT10-9	3052	44	53	200	758

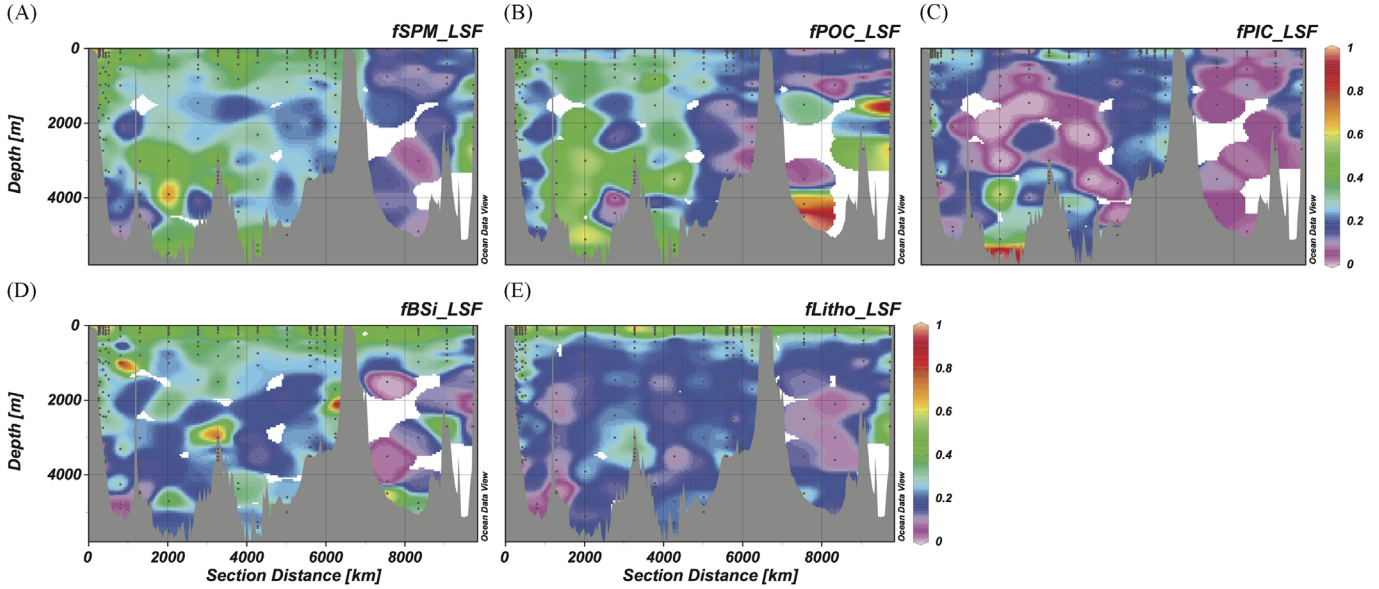

Fig. 4. Full water column section of size partitioning of SPM and major particle phases into the LSF (>51 μm size fraction). (A) SPM (fSPM_LSF), (B) POC (fPOC_LSF), (C) PIC (fPIC_LSF), (D) biogenic silica (fBSi_LSF), (E) lithogenic material (fLitho_LSF). Refer to Fig. 3 for station labels and section map. Note that the SSF PIC for the meridional section (section distance 7000–9000 km) is estimated from a mean PIC:TPC ratio (see Section 2.3.1).

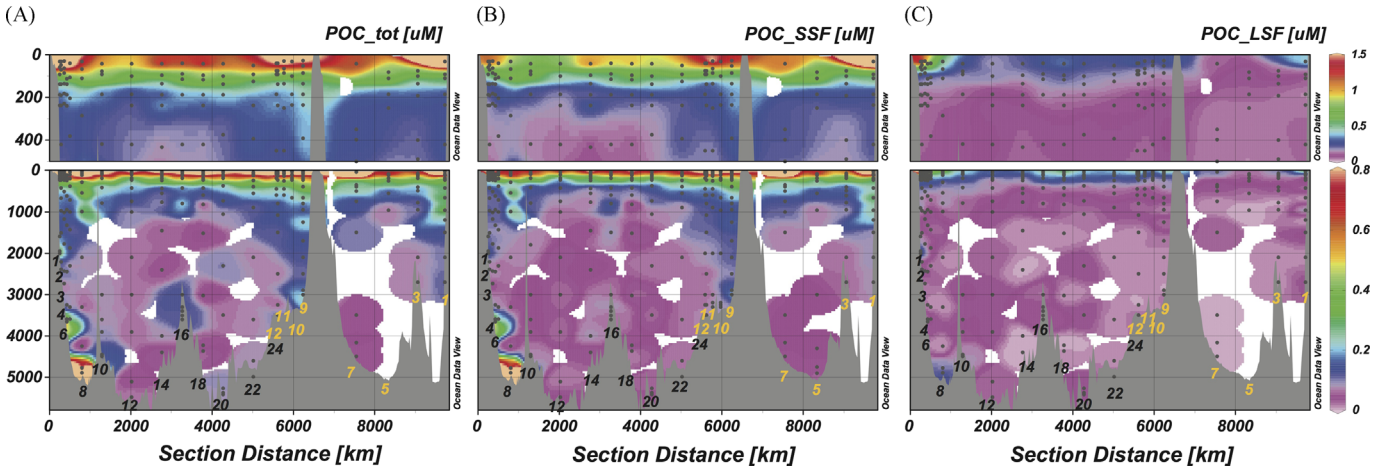

Fig. 5. Section of particulate organic carbon (POC). (A) Total POC (POC_tot); (B) small size fraction (0.8–51 μm) POC (POC_SSF); (C) large size fraction (> 51 μm) POC (POC_LSF). Note that upper 500 m panels are plotted on a different scale than the lower panels. All other plotting conventions as in Fig. 3. POC_tot maxima in the benthic nepheloid layers of GT11-4 and GT11-8 are 0.7 and 2.3 μM, respectively.

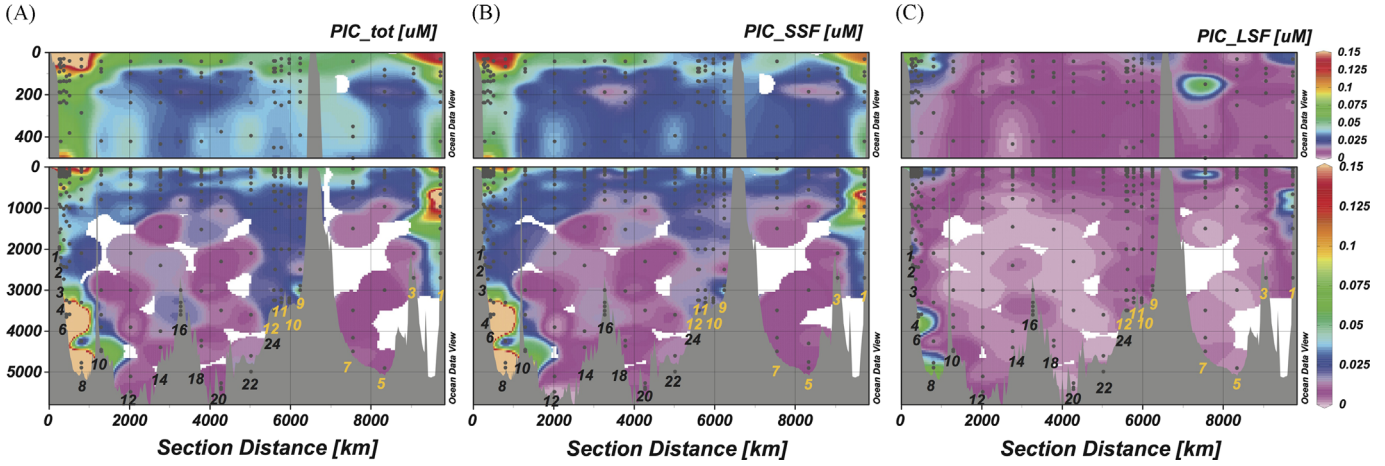

Fig. 6. Section of particulate inorganic carbon (PIC). (A) total PIC (PIC_tot); (B) small size fraction (0.8–51 μm) PIC (PIC_SSF); (C) large size fraction (> 51 μm) PIC (PIC_LSF). PIC_SSF and PIC_tot for meridional stations (GT10-3, 5, 7) were estimated from average PIC:TPC ratios (see Section 2). Plotting conventions as in Fig. 3. PIC_tot maxima in the benthic nepheloid layers of GT11-4 and GT11-8 are 3.2 and 0.7 μM, respectively. Note that the SSF PIC for the meridional section (section distance 7000–9000 km) is estimated from a mean PIC:TPC ratio (see Section 2.3.1).

abundance of diatoms as indicated by the low concentration of biogenic silica.

Upper 100 m BSi was partitioned more to the > 51 μm size fraction (LSF) in the western margin (70 ± 13%) compared to the eastern margin (50 ± 10%). Elevated concentrations of BSi (up to 284 nM at GT11-4) were observed in the benthic nepheloid layers on the western margin.

3.1.2.4. Lithogenic material (Litho). Lithogenic material is the only major particle component that is least abundant in the surface over much of the transect (Fig. 8). It is also the only major component that is not biogenic, and is removed from the surface layer by particle aggregation and sinking (Ohnemus and Lam, 2015). Lithogenic material is strongly enhanced at the margins, especially below 200 m. Median concentrations in the oligotrophic gyre between GT11-10 and GT11-22 in the euphotic zone ($z < 150$ m) and below 200 m were 0.33 ± 0.22 μg/L and 1.14 ± 4.8 μg/L, respectively. At the eastern margin, median concentrations in the euphotic zone and below 200 m were 1.13 ± 1.05 μg/L and 3.47 ± 1.41 μg/L, respectively. The western margin between stations GT11-1 and GT11-8 did not have a near-surface minimum, and median concentrations over the entire water column were 3.62 ± 170 μg/L. The large standard deviation is due to the extremely high enhancements in lithogenic material at the benthic nepheloid layers sampled at GT11-4 and GT11-8, whose concentration maxima reached 1277 and 630 μg/L, respectively. Indeed, lithogenic material is the particle component that was most enhanced at the western margin benthic nepheloid layers. Lithogenic material is partitioned more strongly to the > 51 μm size fraction in the euphotic zone compared to in deep waters (Fig. 4). A detailed examination of the cycling of lithogenic material is presented in Ohnemus and Lam, 2015.

3.1.2.5. Iron and manganese oxyhydroxides. Fe and Mn oxyhydroxides are defined here as excess Fe and Mn over African dust abundances of Fe and Mn using Ti as a tracer of dust. Particulate Fe was almost entirely from crustal material (Ohnemus and Lam, 2015), leaving negligible excess Fe in most of the section, with a few exceptions. There was a slight enhancement of Fe oxyhydroxides in the western margin section between Woods Hole and Bermuda between 1000 and 2000 m (Fig. 9), coinciding with the depth of elevated particulate Fe, Al, and Ti associated with the Labrador Seawater water mass (Ohnemus and Lam, 2015). This apparent Fe oxyhydroxide feature is also observed as elevated labile particulate Fe concentrations (Revels et al., 2015). There was also slight

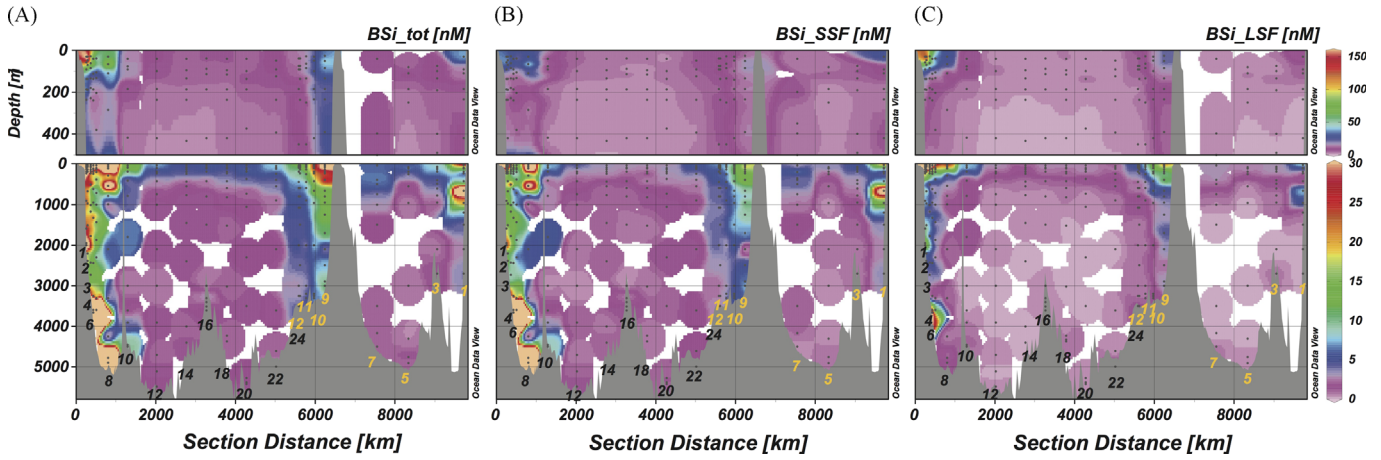

Fig. 7. Section of Biogenic Silica (BSi). (A) Total BSi (BSi_tot); (B) Small size fraction (0.8–51 μm) BSi (BSi_SSF); (C) large size fraction (> 51 μm) BSi (BSi_LSF). Note that upper 500 m panels are plotted on a different scale than the lower panels. Other plotting conventions as in Fig. 3. BSi_tot maxima in the benthic nepheloid layers of GT11-4 and GT11-8 are 476 and 147 nM, respectively. Highest euphotic zone Bsi_tot concentrations were at station GT11-2 (230 nM).

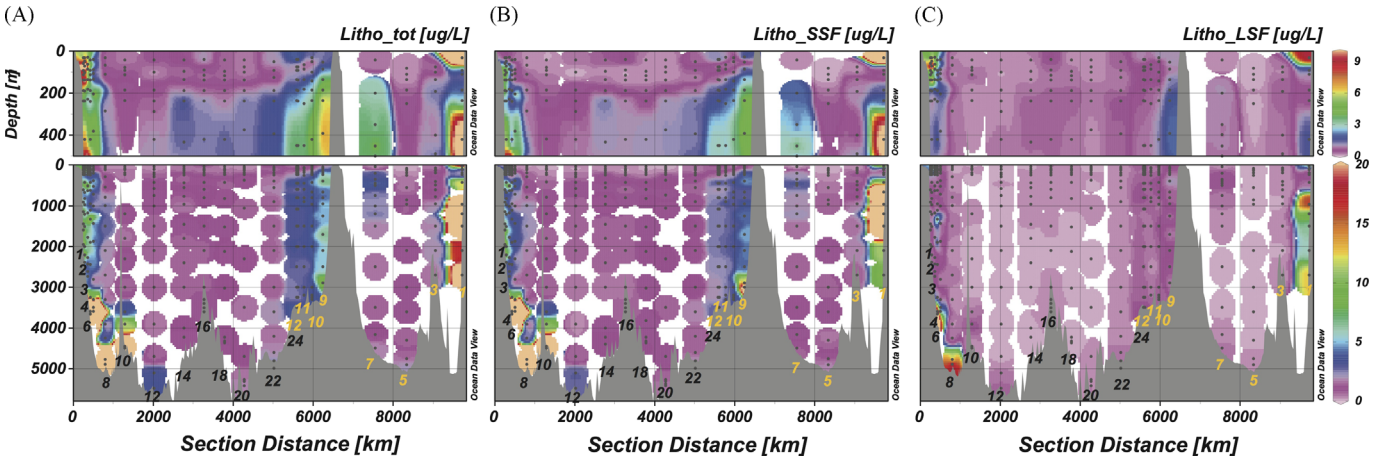

Fig. 8. Section of lithogenic material (Litho). (A) Total Litho (Litho_tot); (B) small size fraction (0.8–51 μm) Litho (Litho_SSF); C) large size fraction (> 51 μm) Litho (Litho_LSF). Note that upper 500 m panels are plotted on a different scale than the lower panels. Other plotting conventions as in Fig. 3. Litho_tot maxima in the benthic nepheloid layers of GT11-4 and GT11-8 are 1276 and 630 μg/L, respectively. Litho_tot maximum at the Mediterranean Outflow at station GT10-1 is 51 μg/L at 1500 m.

enhancement of Fe oxyhydroxides at the nepheloid layers at GT11-4 (1.3 μg/L) and GT10-9 (0.64 μg/L). The most striking enhancement of Fe oxyhydroxides was at the TAG hydrothermal plume at GT11-16, reaching 4.9 μg/L (as $Fe(OH)_3$) at 3300 m in the SSF where it accounted for 52% of the suspended particulate matter mass in the SSF.

Crustal material was not nearly as important a component of total particulate Mn as for Fe, contributing up to 50% of total particulate Mn underneath the Saharan dust plume (GT10-9 to GT10-12) and at the nepheloid layers at Bermuda (GT11-10) and the Mediterranean Outflow (GT10-1), but otherwise contributing generally less than 30% (not shown). Excess Mn (Mn oxyhydroxide) concentrations were low over most of the section. The North American and Iberian margins had higher Mn oxyhydroxides compared to the open ocean by a factor of 2–3. Unlike for Fe oxyhydroxides, the enhancement in Mn oxyhydroxides at the North American margin was strongest in near surface waters, suggesting a possible shallow shelf source. There was an enhancement of Mn oxyhydroxides at both intense western margin nepheloid layers, reaching 2.1 and 1.3 μg/L at stations GT11-4 and GT11-8, respectively, and at the eastern margin nepheloid layer, reaching 0.63 μg/L, but not at the nepheloid layer at BATS (GT11-10). Interestingly, there was no enhancement of Mn oxhydroxides at the TAG hydrothermal plume (see Section 4.1.3), and also no enhancement near the shelf and upper slope of the African margin. Subsurface maxima in Mn oxyhydroxides have been used as a tracer of lateral input from continental margins of North America in the western North Atlantic (Bishop and Fleisher, 1987), Alaska in the eastern Subarctic Pacific (Lam et al., 2006), and Kamchatka in the western Subarctic Pacific (Lam and Bishop, 2008). The absence of Mn oxyhydroxide enhancement at the African shelf and slope could be due to slow oxidation kinetics of reductively mobilized Mn from shelf sediments in the eastern tropical Atlantic oxygen minimum zone, and/or indicate an absence of subsurface lateral transport from the African margin.

The enhancements in Fe and Mn oxyhydroxides in the western margin nepheloid layers were not significant fractions of SPM (Fig. 10). In contrast, the enhancements of both Fe and Mn oxyhydroxides at the eastern (GT10-9) benthic nepheloid layer were a significant fraction of SPM (2.5% of SPM_SSF was $Fe(OH)_3$, and 2.4% of SPM_SSF was MnO_2).

At this and other stations, Fe and Mn oxyhydroxides were predominantly in the 1–51 μm size fraction (SSF) and negligible in the > 51 μm size fraction, consistent with authigenic precipitation of the oxyhydroxides into the SSF.

3.1.3. *Relative particle composition*

Particles were dominated by particulate organic matter (POM) in the euphotic zone, where it accounted for 70 ± 16% (median ± 1 s.d.) of the SSF SPM ((Fig. 10). POM concentrations decreased more quickly than SPM with depth, and accounted for only 24 ± 13% of

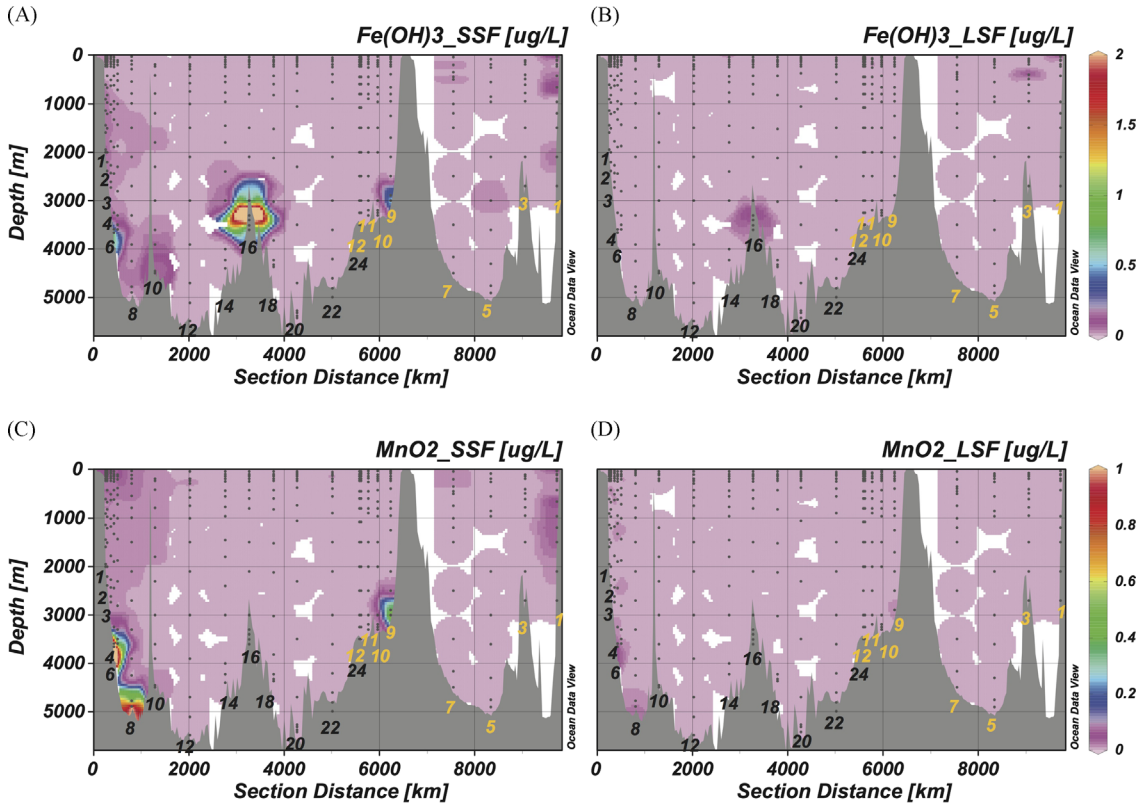

Fig. 9. Full water column section of Fe and Mn oxyhydroxides. Fe oxyhydroxides are calculated as excess Fe over crustal abundances, and are expressed as (A) $Fe(OH)_3$_SSF in the 0.8–51 μm size fraction, (B) $Fe(OH)_3$_LSF in the >51 μm size fraction. Mn oxyhydroxides are calculated as excess Mn over crustal abundances, and are expressed as (C) MnO_2_SSF and (D) MnO_2_LSF. Maximum $Fe(OH)_3$_SSF at the TAG hydrothermal plume at GT11-16 was 4.9 μg/L. Maximum MnO_2_SSF at benthic nepheloid layers at GT11-4 and GT11-8 were 2.1 and 1.3 μg/L, respectively. Plotting conventions as in Fig. 3.

SSF SPM below 1000 m. Overall, POM was a greater contributor to SPM in the LSF (>51 μm) than in the SSF (1–51 μm), especially in the interior of the oligotrophic gyre (Figs. 10 and 11). Lithogenic material had the opposite vertical trend as POM, with a minimum in the euphotic zone (1.6 ± 7.2%), increasing to 40 ± 19% below 1000 m. Lithogenic material dominated all bottom nepheloid layers and the Mediterranean Outflow intermediate nepheloid layer, reaching 70–85% of SSF SPM. Opal was only a significant component of SPM in the euphotic zones at the North American and African margins, where it accounted for up to 24% of LSF SPM, presumably from large diatoms. Opal never exceeded 10% in the SSF. In contrast, $CaCO_3$ was a more important component of SPM in the SSF than the LSF, suggesting that most $CaCO_3$ is from small coccolithophores rather than larger pteropods or foraminifera that would be collected in the LSF. In contrast to POM and lithogenic material, whose relative compositions changed greatly with depth, the relative compositions of opal and $CaCO_3$ were fairly constant with depth.

Compared to compiled particle compositions from available sediment trap data (Chase et al., 2002), SSF particles during the US GEOTRACES North Atlantic Zonal Transect had similar $CaCO_3$ content ($mean_{GT}$=43% vs. $mean_{sed.trap}$=38%), but higher POM ($mean_{GT}$=40% vs. $mean_{sed.trap}$=11%) and lithogenic material ($mean_{GT}$=24% vs. $mean_{sed.trap}$=17%), and much lower opal ($mean_{GT}$=3% vs. $mean_{sed.trap}$=32%).

4. Discussion

4.1. Notable particle features

The US GEOTRACES North Atlantic Zonal Transect was characterized by several notable particle features described above that had SPM concentrations well above surrounding waters: three benthic nepheloid layers on the western (North American) margin and one on the eastern (Mauritanian) margin; the Mediterranean Outflow, which had the highest observed SPM in intermediate waters; and the TAG hydrothermal vent plume at the Mid-Atlantic Ridge (Fig. 12).

4.1.1. Benthic nepheloid layers (BNLs)

Enhanced SPM concentrations in BNLs could affect scavenging of particle-reactive TEIs by providing more surface area for scavenging removal and by affecting the partition coefficient (K_d) of particle-reactive TEIs between the dissolved and particulate phase, if the composition of the particles in the BNLs are different than particles in the water column (Rutgers van der Loeff and Boudreau, 1997).

Strong BNLs were sampled by the in-situ pumps near the Mauritanian margin at station GT10-9, and near the North American margin at stations GT11-4, GT11-8, and GT11-10 (Figs. 3 and 12). The occurrence of BNLs was likely much more common, however, since the pumps were not always able to sample them. On the first cruise (GT10), the lack of an altimeter prevented near-bottom sampling, whereas on the second cruise, strong western bottom boundary currents induced significant wire angles (up to 40° at GT11-6), which prevented near-bottom sampling. Indeed, the transmissometer on the GEOTRACES rosette showed at least slight near-bottom reduction of beam transmission (and thus increases in particle concentrations) at most stations on both cruises, but station GT11-6 had the only intense BNL not sampled by the pumps. Integrated SPM was estimated by summing the products of the SPM and the thickness of the layer to the next observation below (or ocean bottom), starting at the depth where SPM was above the clear water minimum background. The variable depths above bottom at which the pumps sampled the BNLs at each

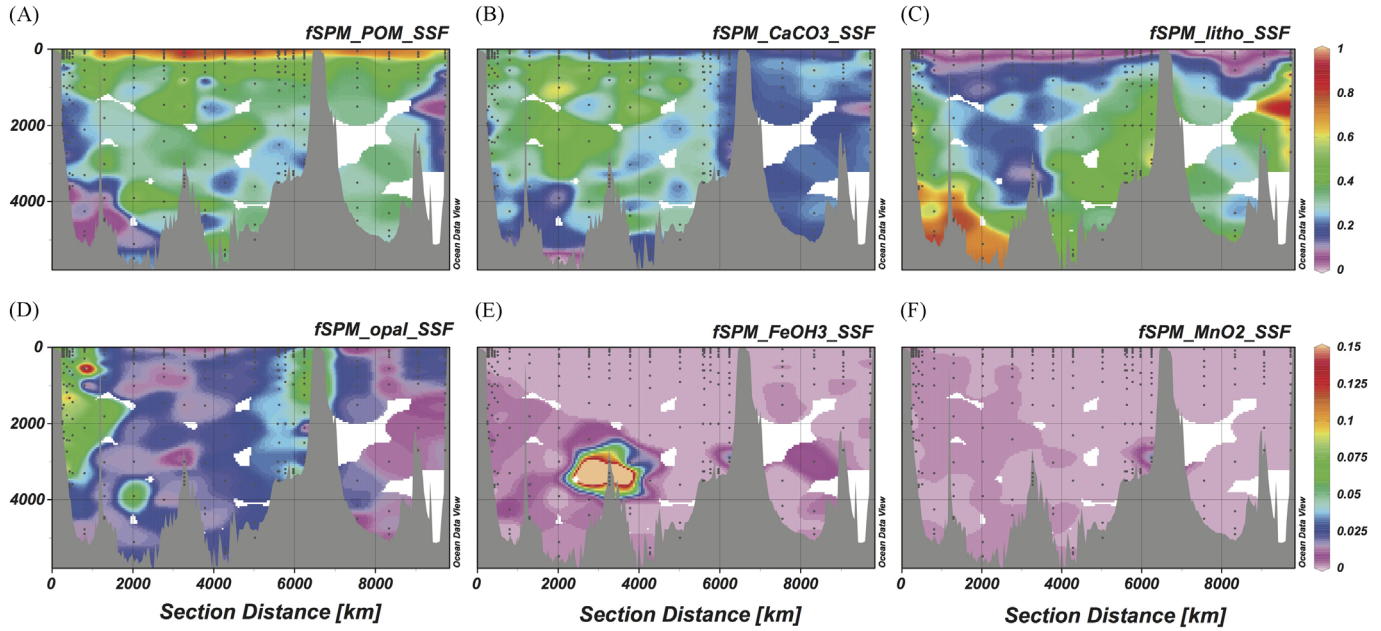

Fig. 10. Relative composition of SPM in the SSF (< 51 μm) for (A) particulate organic matter (fSPM_POM_SSF), (B) $CaCO_3$ (fSPM_CaCO3_SSF), (C) lithogenic material (fSPM_Litho_SSF), (D) opal (fSPM_opal_SSF), E) Fe oxyhydroxides (fSPM_FeOH3_SSF), and F) Mn oxyhydroxides (fSPM_MnO2_SSF). Note that the relative compositions in the top row (A–C) are plotted on a different color scale than the bottom row (D–F). Maximum $Fe(OH)_3$ was 0.52 at the TAG hydrothermal plume at GT11-16. Refer to Fig. 3 for station labels and section map. Note that the SSF $CaCO_3$ for the meridional section (section distance 7000–9000 km) is estimated from a mean PIC:TPC ratio (see Section 2.3.1).

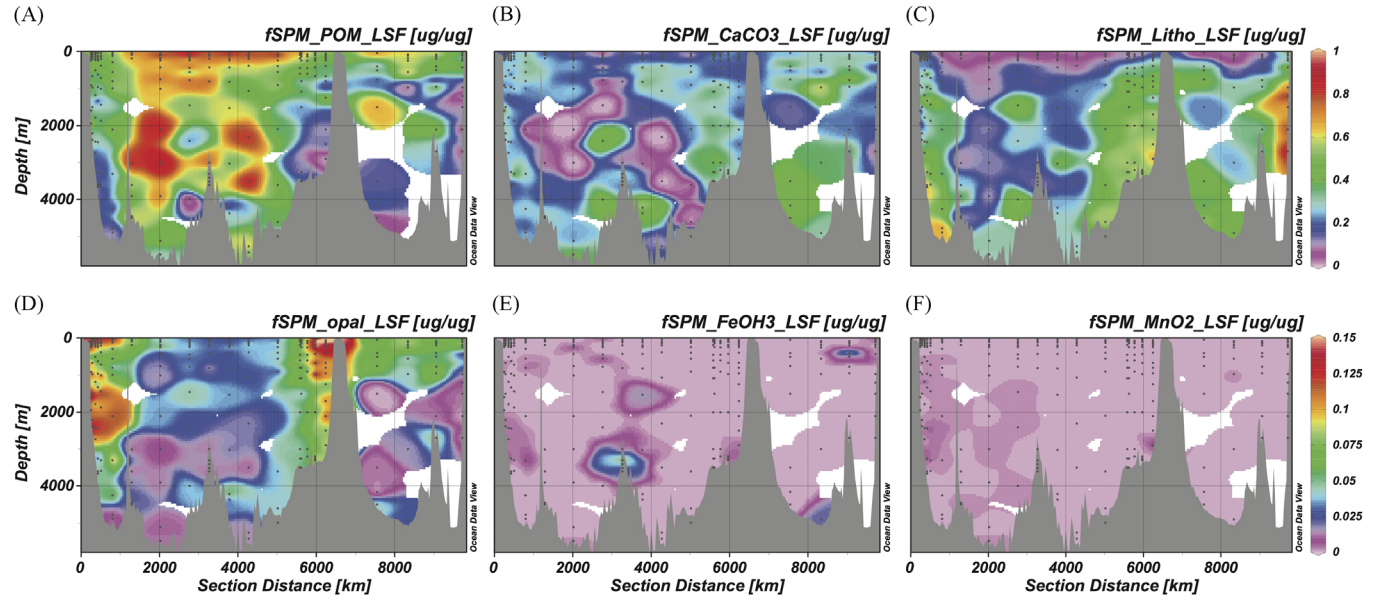

Fig. 11. Relative composition of SPM in the LSF (> 51 μm). Note that the compositions of (A) particulate organic matter (POM), (B) $CaCO_3$, and (C) lithogenic material (Litho) are plotted on a different color scale than (D) opal, (E) Fe oxyhydroxides ($FeOH_3$), and (F) Mn oxyhydroxides (MnO_2).

station (Table 2) and the relatively coarse depth resolution in the near-bottom pumps introduces error in the absolute estimated maximum and integrated SPM of the BNLs at each station. Our method of integration likely underestimates the true integrated SPM, but the relative ranking of the strength of the BNLs sampled is likely unaffected. Station GT11-4 had by far the most intense BNL and highest SPM of the section, with a maximum SPM_{TOT} of 1648 μg/L, and an integrated SPM_{TOT} of 28 mg/cm^2, followed by GT11-8, then GT11-10, and finally GT10-9 at 4.7, 2.9, and 0.76 mg/cm^2, respectively (Table 2).

Given that the maximum SPM_{TOT} at GT11-4 was sampled on average 130 m from the bottom because of the wire angle during pumping, the intensity of the BNL at this station may be comparable to the highest SPM_{TOT} recorded during the High Energy Benthic Boundary Layer Experiment (HEBBLE) of 5000 μg/L, just 4 m above the bottom, at the nearby Nova Scotian Rise at 4880 m water depth (Gross et al., 1988). Station GT11-8 was in 4928 m waters and was sampled only 39 m above the bottom, but had a far lower maximum SPM concentration (763 μg/L; Table 2) than GT11-4. Time-series measurements during the HEBBLE project showed that sites in this area can exhibit order of magnitude variations in the suspended particulate load over the course of only a few days (Gardner and Sullivan, 1981; Gross et al., 1988), so it is possible that the time-averaged intensity of the BNLs at each of the stations could be quite different than our sampling indicates.

Beam transmission profiles show that three of the sampled BNLs were 100–300 m thick, whereas the BNL at station GT11-10 (31.9°N, 64.1°W) near Bermuda was around 1100 m thick (Fig. 13). The

maximum intensity was only 40 μg/L, about 20 times lower than that at GT11-8 (Fig. 12), but its considerably greater thickness and gentle gradient leads to an integrated sediment load (2.9 mg/cm^2) that is only 40% lower than that at GT11-8 (Table 2). A BNL of similar intensity (max SPM=25–50 μg/kg) and thickness (~1000 m) was previously observed during the GEOSECS Western Atlantic section at around 35°N, 45°W, slightly north and further east of GT11-10 (Brewer et al., 1976). A plume of elevated near-bottom particulate standing crop of 2–3 mg/cm^2, similar to GT11-10, was also observed in the Lamont Doherty Geological Observatory (LDGO) nephelometer dataset at 35°N extending between 70°W and 45°W (Biscaye and Eittreim, 1977). A thick BNL plume in this part of the Atlantic thus seems to be a reproducible feature. Brewer et al. (1976) observed that the thick BNL was associated with a nutrient front and a relief of strong near-bottom density gradients, hypothesizing that the latter allowed particles to disperse up to 1 km off the bottom. While we also observe a gentle near-bottom density profile at GT11-10, a gentle density gradient is not sufficient for a thick BNL, since the near-bottom density profile at GT11-8, which had a typically thin BNL, was almost identical to the one at GT11-10 (Fig. 13). The source of particles hundreds of meters above the bottom at GT11-10 may thus be at least partly laterally supplied from a nearby topographic feature such as the Bermuda Rise (cf. McCave, 1986).

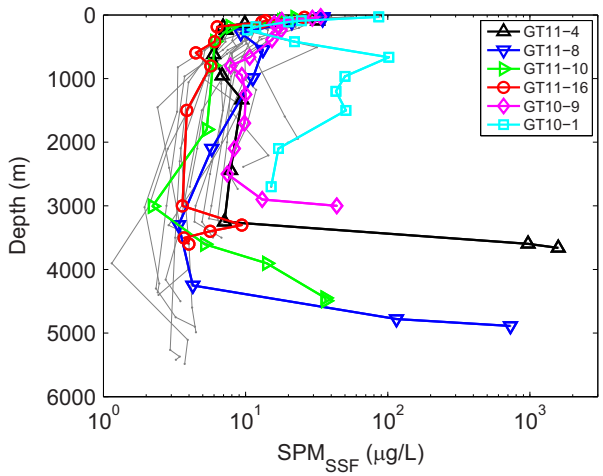

Fig. 12. Profiles of SPM$_{SSF}$ (μg/L) (<51 μm) highlighting stations with notable profiles. Nepheloid layers are at stations GT11-4 (black up triangle), GT11-8 (blue down triangle), GT11-10 (green right triangle), and GT10-9 (magenta diamond). The TAG hydrothermal plume is at station GT11-16 (red circle). The Mediterranean Outflow turbidity plume is at station GT10-1 (cyan squares). All other profiles in the section are plotted as thin grey lines in the background. Note the logarithmic *x*-axis scale. (For interpretation of the references to color in this figure legend, the reader is referred to the web version of this article.)

The sampled BNLs provide an opportunity to compare the compositions of particles in BNLs with those in the surrounding water column to assess the role of particle composition in scavenging removal of TEIs. The particles in all sampled BNLs were partitioned more strongly into the SSF (93 ± 4%) compared to the rest of the section (78 ± 11%) (Fig. 4). All western margin BNLs were characterized by strongly enhanced relative lithogenic composition (79 ± 5%) in the SSF and a corresponding relative decrease in all other components compared to particles in the water column above (Fig. 14). The LSF of the BNLs are never as rich in lithogenics as the SSF, reflecting the contribution of lithogenic-poor LSF particles sinking from above (Fig. 14). Station GT11-10 is an extreme example of this, with a far lower relative lithogenic composition in the LSF

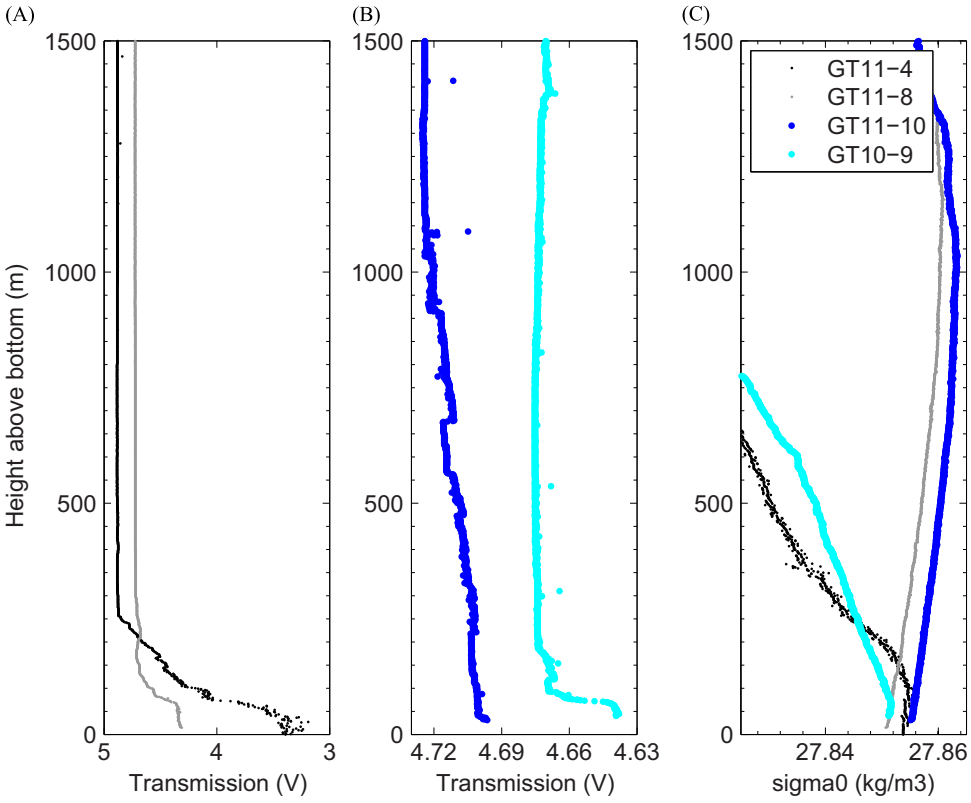

Fig. 13. Thickness of benthic nepheloid layers from (A and B) transmission and (C) density (plotted as sigma0) at stations GT11-4 (small black dots), GT11-8 (small gray dots), GT11-10 (large blue dots), and GT10-9 (large cyan dots). Transmission (volts) and density data from the GEOTRACES rosette CTD except for station GT11-4, which were from the pump CTD. Note that transmission is plotted in reverse so that increasing particle concentration is to the right (lower transmission). Transmission between instruments and between cruises has not been calibrated, and is plotted simply to indicate the thickness of BNLs relative to the clearwater background. (For interpretation of the references to color in this figure legend, the reader is referred to the web version of this article.)

(10–38%) compared to the SSF (59–80%) or to the LSF at the other nepheloid stations. This suggests that there is more exchange (aggregation and disaggregation) between the two size fractions in the thin, concentrated BNLs compared to the thick and more dilute BNL at station GT11-10 (cf. McCave, 1986).

Unlike the western margin BNLs, where the relative lithogenic composition can be used to define the presence of a nepheloid layer, the lithogenic composition of the BNL at station GT10-9 is not significantly different than the water column above it (Fig. 14). What distinguishes this BNL is the presence of significant Fe and Mn oxyhydroxides, strongly suggesting reductive mobilization of Fe and Mn from suboxic sediments at this margin. The relative abundance of Fe and Mn oxyhydroxides at station GT10-9 was highest not at the deepest (3000 m) pump closest to (50 m above) the bottom, but at the next pump above it (2900 m), 150 m above the bottom. The density profile shows that this second pump was above the 75 m benthic boundary layer (Fig. 13), suggesting that the Fe and Mn in this sample was advected laterally from shallower slope sediments, rather than originating from the sediments directly below (cf. Sarmiento and Rooth, 1980).

Although it appears that Mn oxyhydroxides are observed at all BNLs (Fig. 9), it is only at the Mauritanian BNL at station GT10-9 where their relative concentrations increase and they become a significant component (2.4%) of the overall particle composition. The elevated Mn oxyhydroxides observed at the western boundary BNLs are swamped out by much higher SPM loads, so they remain an insignificant fraction of the overall particle composition. Fe oxyhydroxides are also significant (2.5%) at the BNL at GT10-9. The presence of Fe and Mn oxyhydroxides makes the nepheloid layer at the Mauritanian margin unique in this transect and likely to affect scavenging of particle-reactive TEIs differently than other BNLs.

4.1.2. Mediterranean outflow

The highest mid-water column SPM was observed at station GT10-1 at the Iberian margin, between 665 and 1500 m (Fig. 3), coinciding with high salinity Mediterranean Outflow waters. This is a persistent turbidity feature that originates with the resuspension of particles from the Strait of Gibraltar and the slope sediments of the Gulf of Cadiz (McCave and Hall, 2002; Thorpe, 1972). Like western margin BNLs, these particles are characterized by high lithogenic composition (Figs. 10 and 11). Although the salinity at GT10-1 indicates that the Mediterranean Outflow waters have not been very diluted with lower salinity North Atlantic water, the maximum SPM load observed (SPM_{SSF} = 102 μg/L) is already well below those previously observed closer to the particle source region (~250 μg/L), confirming rapid particle fallout from this water mass as it travels northward along the Iberian margin and out into the North Atlantic (McCave and Hall, 2002). The high SPM load combined with rapid vertical removal explains the mid-water deficit in total ^{234}Th activity observed at this station (Owens et al., 2015).

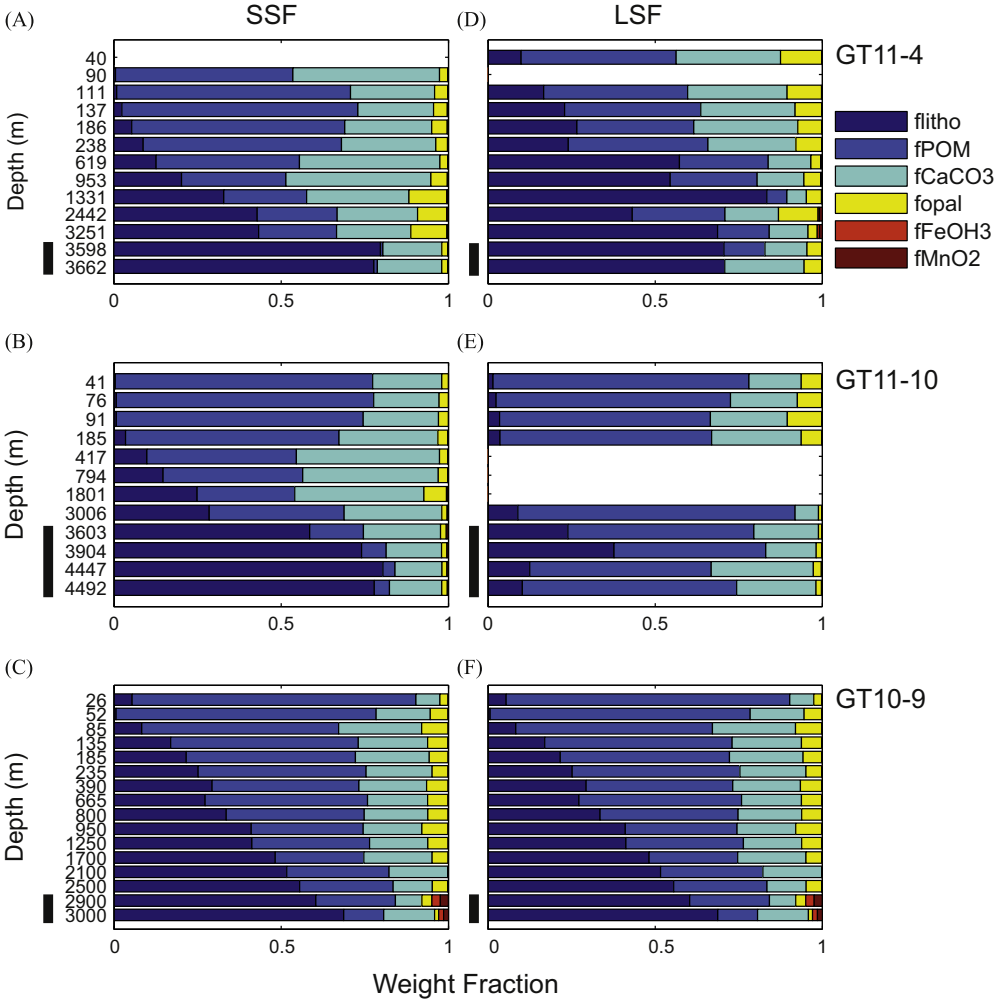

Fig. 14. Profiles of size-fractionated relative particle composition at three stations containing benthic nepheloid layers. (A–C) Small size fraction (SSF; < 51 μm); (D–F) Large size fraction (LSF; > 51 μm). Thick vertical bars indicate the depths of the nepheloid layers at each station ((A) and (D): GT11-4; (B) and (E): GT11-10; (C) and (F): GT10-9). Station GT11-8 not shown but similar to GT11-4. The tradeoff between POM and lithogenic material with depth can be clearly seen in the SSF particles.

4.1.3. TAG hydrothermal plume

There has been extensive work on the chemistry of suspended particles in the TAG hydrothermal plume, focusing on particulate iron and the role of Fe oxyhydroxides in scavenging other trace elements (German et al., 1991; Trefry et al., 1985; Trocine and Trefry, 1988). Our work confirms the importance of Fe oxyhydroxides in the TAG hydrothermal plume, but also shows that almost half of the SPM mass is comprised of other particle phases. After Fe oxyhydroxides (52%), POM is the next most important (22%), followed by $CaCO_3$ (18%), lithogenic material (6%), and opal (2%) (Fig. 15). Calcium carbonate, lithogenic material, and most of the POM are present from the background SPM that is mixed in with the hydrothermal plume particles, but some of the POM, most of the opal, and virtually all of the Fe oxyhydroxides are generated by hydrothermal vent processes. The role of POC in hydrothermal plumes has lately received more attention, as POC has been proposed to help stabilize Fe(II) from oxidation, thus allowing reduced iron to persist far longer than expected from oxidation kinetics (Toner et al., 2009).

BSi_{TOT} was enhanced by a factor of ~4 to 3.9 nM in the hydrothermal plume compared to particles above and below the plume. This is presumably amorphous silica precipitated abiotically from vent fluids that is accessed by our alkaline leach method (German and Von Damm, 2003). Even though opal is a very minor component of SPM_{SSF} at the plume, it is the only phase besides Fe oxyhydroxide that exhibits an increase in relative concentration compared to the waters above and below the plume (Fig. 15).

Mn oxyhydroxides were negligible, and in fact exhibited a puzzling decrease at the hydrothermal plume compared to background levels (Fig. 15). This decrease is also observed in total particulate Mn, and so is not an artifact of the MnO_2 calculation. (German et al., 1991) observed that Ca and Mn were the only elements out of 18 measured that persisted in solution at TAG, but they nonetheless observed a positive correlation between particulate Fe and Mn. The lack of a positive correlation in our data can be partly explained by the different oxidation kinetics of Fe and Mn: the oxidation half-life of Fe^{2+} at TAG is only 2.1 min (Rudnicki and Elderfield, 1993), whereas Mn oxidation is slow enough that dissolved Mn is used as a conservative tracer for vent fluid dilution close to the vent (Rudnicki and Elderfield, 1992). Our sampling appeared to be closer to the vent source than the German et al. (1991) samples, where Fe oxidation was taking place but not Mn oxidation. However, this does not explain the decrease in MnO_2 concentration. Based on dissolved Mn concentrations in vent fluids (0.7 mM) (Chiba et al., 2001) and measured in the plume during our occupation (~30 nM) (Hatta et al., 2015), we estimate a vent fluid dilution factor of ~23,000x at our plume sampling site. Given such a large dilution factor, we cannot explain the factor of 2 decrease in MnO_2 simply with dilution of background MnO_2 with MnO_2-free vent fluid. Mn is the only particulate component whose absolute concentration decreases in the plume, and also the only transition metal whose partition coefficient decreases significantly compared to the water column above the plume ($K_{d\text{plume}}/K_{d1500\ \text{m}}=0.002$). The uniqueness of the behavior of Mn argues against a particle removal process, which would be expected to remove other elements as well. Instead, the decrease in MnO_2 appears to be due to a change in chemistry or microbial activity of the plume water compared to the water column above that significantly shifts the partitioning of Mn away from particles and toward the dissolved phase. We unfortunately cannot determine the exact mechanism from our data.

4.2. Ballast correlations

The "ballast hypothesis" was proposed to explain observed correlations between POC and $CaCO_3$ flux from sinking particles collected in deep (>2000 m) sediment traps (Armstrong et al., 2002; François et al., 2002; Klaas and Archer, 2002). One

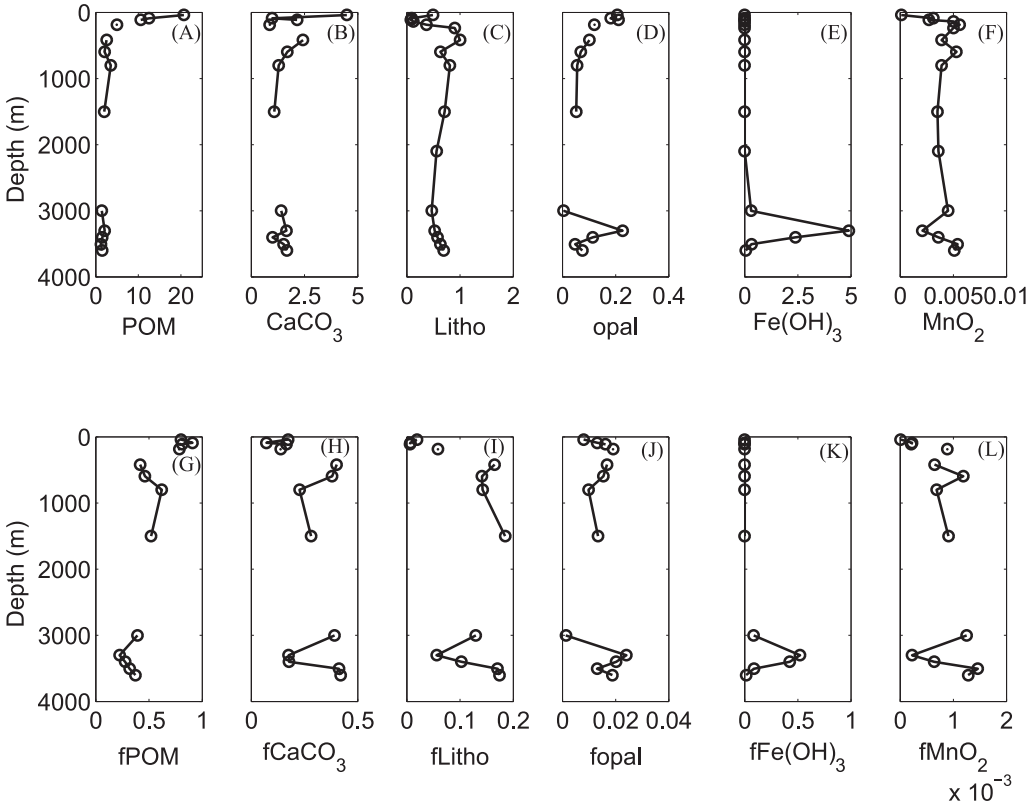

Fig. 15. Profiles of absolute (top row, A–F) and relative (bottom row, g^{-1}) particle composition in the SSF (<51 μm) at the TAG hydrothermal plume station (GT11-16). All absolute particle composition concentrations are in μg/L. The plume is best defined by $Fe(OH)_3$.

explanation for the observed ballast mineral correlation in deep sediment traps is that there is a $CaCO_3$-associated "protected" POC fraction (Armstrong et al., 2002). Total POC is thus composed of this mineral-associated fraction, which constitutes a small fraction of total POC in the upper water column, and a labile, or "free" POC fraction, which remineralizes quickly through the mesopelagic. Other proposed mechanisms are that $CaCO_3$ provides excess density to sinking aggregates, and/or affect aggregate packaging, and thus increase settling velocity (Engel et al., 2009; Iversen and Ploug, 2010; Klaas and Archer, 2002), or that more oligotrophic $CaCO_3$-producing regions export POC that is more resistant to degradation than diatom-producing regions (François et al., 2002).

Recent investigations have searched for the source of the POC–$CaCO_3$ correlation in the upper water column using large size fraction particles (Lam and Bishop, 2007; Lam et al., 2011), snow-catchers (Riley et al., 2012), the ^{238}U–^{234}Th disequilibration method (Le Moigne et al., 2012; Thomalla et al., 2008), and empirical models of global datasets (Henson et al., 2012). Results have been decidedly equivocal, with analyses of time-series or regionally specific data often showing no ballast correlations

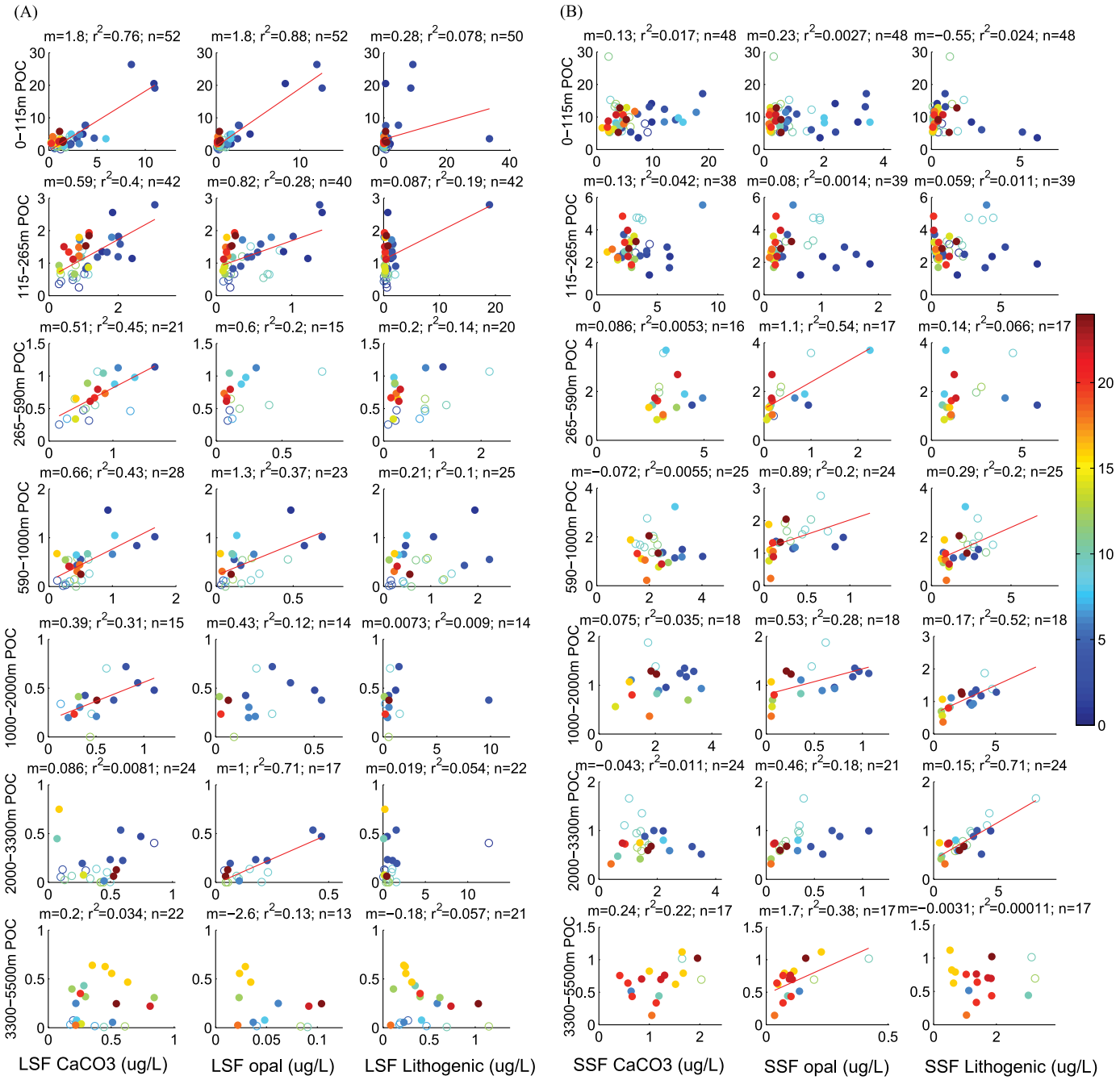

Fig. 16. Scatterplots of POC and ballast minerals $CaCO_3$ (1st column), opal (2nd column), and lithogenic material (3rd column) for samples in 7 depth bins from the euphotic zone (top row) to the deepest 2200 m (bottom row) for (A) LSF (>51 μm) and (B) SSF (1–51 μm). Colorbar represents station number; first and second cruise plotted as open and closed circles, respectively. All bottom and intermediate nepheloid layer samples were excluded by plotting only those samples where Litho_SSF <10 μg/L. The slope (m), coefficient of determination (r^2), and sample size (n) of linear least squares fits are indicated above each panel. Only significant ($p<0.05$) linear fits are plotted (red line). Note that a high lithogenic outlier ($\sim$10 μg/L) in each of the 1000–2000 m and 2000–3300 m depth bins is not shown for LSF panels. (For interpretation of the references to color in this figure legend, the reader is referred to the web version of this article.)

Table 3
Ballast mineral correlations. Regression statistics from multiple linear regressions between size-fractionated suspended POC and ballast minerals from the US GEOTRACES North Atlantic Zonal Transect (this work), compared to a previous global compilation (Lam et al. 2011). Slopes from the multiple linear regressions are also referred to as "carrying coefficients". Significant ($p < 0.05$) regressions are in bold. Please note that the Lam et al. 2011 coefficients and statistics are slightly different than previously published due to correction of a data error.

Depth range (m)	Size fraction	Multiple linear regressions					
		$CaCO_3$ slope ($\pm$95% CI)	Opal slope ($\pm$95% CI)	Lithogenic slope ($\pm$95% CI)	R^2	p	No. of obs.
North Atlantic (this study)							
0–115	> 51 μm	**0.14 ± 0.55**	**1.71 ± 0.51**	**−0.07 ± 0.11**	**0.88**	**< 0.001**	**50**
115–265	> 51 μm	**0.38 ± 0.43**	**0.20 ± 0.66**	**0.03 ± 0.06**	**0.39**	**< 0.001**	**40**
265–590	> 51 μm	**0.84 ± 0.56**	**−0.32 ± 1.72**	**0.29 ± 0.60**	**0.75**	**0.002**	**14**
590–1000	> 51 μm	**0.51 ± 0.66**	**0.32 ± 1.45**	**0.10 ± 0.25**	**0.48**	**0.008**	**22**
1000–2000	> 51 μm	0.66 ± 0.89	−0.50 ± 1.79	0.01 ± 0.08	0.33	0.286	13
2000–3300	> 51 μm	**−0.16 ± 0.60**	**1.18 ± 0.66**	**−0.01 ± 0.13**	**0.74**	**0.002**	**15**
3300–5500	> 51 μm	0.45 ± 0.78	−1.28 ± 9.0	−0.21 ± 0.89	0.27	0.400	13
> 1000	> 51 μm	**0.32 ± 0.34**	**0.53 ± 0.6**	**0.02 ± 0.09**	**0.26**	**0.006**	**44**
> 2000	> 51 μm	0.37 ± 0.43	0.55 ± 0.73	−0.11 ± 0.18	0.25	0.070	28
LSF global compilation (Lam et al. 2011)							
0–115	> 53 μm	**0.72 ± 0.37**	**0.17 ± 0.05**	**N/A[a]**	**0.32**	**< 0.001**	**169**
115–265	> 53 μm	**0.45 ± 0.15**	**0.06 ± 0.04**	**N/A[a]**	**0.34**	**< 0.001**	**102**
265–590	> 53 μm	**0.35 ± 0.2**	**0.04 ± 0.04**	**N/A[a]**	**0.14**	**< 0.001**	**113**
590–1000	> 53 μm	**0.48 ± 0.31**	**−0.02 ± 0.06**	**N/A[a]**	**0.09**	**0.011**	**97**
Sediment trap global compilation (Klaas and Archer 2002)							
> 1000 m	Sediment trap	**0.094 ± 0.01**	**0.025 ± 0.01**	**0.035 ± 0.01**	**0.93**	**< 0.001**	**107**
> 2000 m	Sediment trap	**0.075 ± 0.01**	**0.029 ± 0.01**	**0.052 ± 0.02**	**0.95**	**< 0.001**	**78**

[a] The Lam et al. 2011 analysis was restricted to open ocean regions with assumed low lithogenics, and so did not include lithogenics in the regressions

(Boyd and Trull, 2007), or widely varying ballast mineral carrying coefficients (Wilson et al., 2012).

In the mineral protection model, one would not expect a correlation between POC and $CaCO_3$ export flux at the base of the euphotic zone since POC is dominated by the free POC fraction. It is only through the removal of the free POC fraction through remineralization in the mesopelagic that the underlying $CaCO_3$-associated protected POC fraction is revealed in the bathypelagic. A consequence of this "mineral protection" conceptual model is that one would expect a strengthening of the correlation between POC and $CaCO_3$ with increasing depth as the free POC was remineralized. Because of insufficient depth resolution in global or regional datasets of particle flux, this hypothesis is difficult to examine directly with sinking particles from sediment traps. Although LSF particles are defined by size and are thus not the same as sinking particles collected by sediment traps, it is nonetheless the size fraction that is more likely to contain sinking particles and provide an alternative to examine changes in the strength of correlation with depth.

Here we use the > 51 μm LSF particles from in-situ pumping as a proxy for sinking particles to test the hypothesis that mineral ballast correlations should strengthen with depth in the LSF. We divide the water column into seven depth bins of increasing thicknesses to compensate for decreasing sampling resolution with depth, and perform single (Fig. 16) and multiple linear regressions (Table 3) in each depth bin. In keeping with previous papers' conventions, we use "carrying coefficient" to be the coefficients of the multiple linear regressions between POC and ballast minerals (Klaas and Archer, 2002; Lam et al., 2011; Wilson et al., 2012). We also examine the POC—ballast mineral associations in the < 51 μm SSF particles (Fig. 16). The degree of similarity between the two size classes can indicate the level of exchange between the two classes by aggregation and disaggregation processes (Abramson et al., 2010; Wakeham and Canuel, 1988).

LSF POC is significantly correlated with LSF $CaCO_3$ in all depth bins in the upper 2000 m, but not in the two depth bins below 2000 m (Fig. 16A). In comparison, SSF POC is not correlated with SSF $CaCO_3$ in any of the depth bins (Fig. 16B). The breakdown in the LSF correlation below 2000 m suggests an association that is set in the upper water column, but that breaks down as POC is remineralized, rather than a mineral protection mechanism. The correlation in the LSF but not the SSF further suggests that the association of POC–$CaCO_3$ is established by carbonate-producing grazers (e.g., pteropods and/or foraminifera) that would be found in the large size fraction, rather than by carbonate-producing phytoplankton (e.g., coccolithophores) that would be expected to be in the small size fraction. The estimated carrying coefficient of $CaCO_3$ for POC in > 1000 m LSF particles is higher than for global sediment traps (Klaas and Archer, 2002), but is so poorly constrained that they are the same within error (Table 3).

POC was inconsistently correlated with opal in both the LSF and the SSF, depending on depth bin (Fig. 16). LSF POC showed no correlation with LSF lithogenic material except in the upper most depth bin, which was driven by a few high points. Several studies have suggested the importance of lithogenic material as ballasting agents, especially in the North Atlantic and Mediterranean where the influence of Saharan dust is important (Bressac et al., 2014; Dunne et al., 2007; Lima et al., 2013; Ternon et al., 2010), but these were all modeling studies or time-series studies at a single location. The data from our transect show no geographical relationship between POC and lithogenic material in the LSF. Between 590 and 2000 m, there is a significant correlation between POC and lithogenics in the SSF, explaining up to 71% of the variance in SSF POC in the 2000–3300 m depth range (Fig. 16B). The stations that define this correlation are GT10-9 on the eastern margin and the line W stations on the western margin (Fig. 16B, light blue open circles and dark blue filled circles, respectively). Lithogenic particles from this depth range in the western margin are likely associated with resuspended particles transported by Labrador Seawater (Ohnemus and Lam, 2015). Likewise, there is iron isotope evidence of lateral transport in this depth range at GT10-9 on the eastern margin (Revels et al., 2015). The SSF POC-lithogenic correlation at these intermediate depth ranges may thus indicate a transported signal from continental margin sediments.

5. Conclusions

SPM in the US GEOTRACES North Atlantic Zonal Transect exhibited a three order of magnitude range in concentration (2.2 μg/L in the oligotrophic interior to 1648 μg/L in the western benthic nepheloid layers). SPM in the North Atlantic basin is

characterized by high relative concentrations of particulate organic matter and lithogenic material, average $CaCO_3$, and very low opal.

In this North Atlantic dataset, the mineral ballast correlations with POC in the LSF are not strong, indicated by the poorly constrained carrying coefficients, and correlations in the SSF are generally poor. The lack of strong correlations within this regional dataset is consistent with the notion that ballast mineral correlations with POC only emerge in global datasets that combine different biogeochemical provinces (cf. Boyd and Trull, 2007; Wilson et al., 2012).

Acknowledgements

Many thanks to the chief scientists (E. Boyle, W. Jenkins, G. Cutter) and the scientific and ship's crew of the R/V Knorr during these voyages. Special thanks to Paul Morris, Steve Pike, Stephanie Owens, Sylvain Rigaud, Kuanbo Zhou, Sara Rauschenberg for help at sea; Matt Charette and Ken Buesseler for pump coordination and collaboration; Steve Manganini, Tom Ireland, Rick Murray for PIC analyses; Janeea Ventour and Courtnee DePass for biogenic Si analyses; Paul Henderson, Stephanie Owens, and Crystal Breier for POC analyses; and the US and International GEOTRACES Offices (NSF OCE-0850963 and OCE-1129603) for project support. Thanks to two anonymous reviewers whose comments helped to improve the manuscript. This work was funded by NSF OCE-0963026 to PJL.

References

Abramson, L., Lee, C., Liu, Z.F., Wakeham, S.G., Szlosek, J., 2010. Exchange between suspended and sinking particles in the northwest Mediterranean as inferred from the organic composition of in situ pump and sediment trap samples. Limnol. Oceanogr. 55 (2), 725–739. http://dx.doi.org/10.4319/lo.2009.55.2.0725.

Armstrong, R.A., Lee, C., Hedges, J.I., Honjo, S., Wakeham, S.G., 2002. A new, mechanistic model for organic carbon fluxes in the ocean based on the quantitative association of POC with ballast minerals. Deep-Sea Res. Part II—Topical Stud. Oceanogr. 49 (1–3), 219–236.

Bacon, M.P., Anderson, R.F., 1982. Distribution of thorium isotopes between dissolved and particulate forms in the Deep Sea. J. Geophys. Res. 87 (C3), 2045–2056.

Barrett, P.M., Resing, J.A., Buck, N.J., Feely, R.A., Bullister, J.L., Buck, C.S., Landing, W.M., 2014. Calcium carbonate dissolution in the upper 1000 m of the eastern North Atlantic (2013GB004619). Global Biogeochem. Cycles 28, http://dx.doi.org/10.1002/2013GB004619.

Biscaye, P.E., Eittreim, S.L., 1977. Suspended particulate loads and transports in the nepheloid layer of the abyssal Atlantic Ocean. Mar. Geol. 23 (1–2), 155–172.

Bishop, J.K., 1991. Getting good weight. Geophys. Monogr. Ser. 63, 229–234.

Bishop, J.K.B., Edmond, J.M., Ketten, D.R., Bacon, M.P., Silker, W.B., 1977. Chemistry, biology, and vertical flux of particulate matter from upper 400 M of equatorial Atlantic Ocean. Deep-Sea Res. 24 (6), 511–548.

Bishop, J.K.B., Fleisher, M.Q., 1987. Particulate manganese dynamics in Gulf-Stream warm-core rings and surrounding waters of the NW Atlantic. Geochim. Cosmochim. Acta 51 (10), 2807–2825.

Bishop, J.K.B., Lam, P.J., Wood, T.J., 2012. Getting good particles: accurate sampling of particles by large volume in-situ filtration. Limnol. Oceanogr. Methods 10, 681–710. http://dx.doi.org/10.4319/lom.2012.10.681.

Boyd, P.W., Trull, T.W., 2007. Understanding the export of biogenic particles in oceanic waters: is there consensus? Prog. Oceanogr. 72 (4), 276–312.

Bressac, M., Guieu, C., Doxaran, D., Bourrin, F., Desboeufs, K., Leblond, N., Ridame, C., 2014. Quantification of the lithogenic carbon pump following a simulated dust-deposition event in large mesocosms. Biogeosciences 11 (4), 1007–1020. http://dx.doi.org/10.5194/Bg-11-1007-2014.

Brewer, P.G., Spencer, D.W., Biscaye, P.E., Hanley, A., Sachs, P.L., Smith, C.L., Kadar, S., Fredericks, J., 1976. The distribution of particulate matter in the Atlantic Ocean. Earth Planet. Sci. Lett. 32 (2), 393–402. http://dx.doi.org/10.1016/0012-821x(76)90080-7.

Brzezinski, M.A., Nelson, D.M., 1995. The annual silica cycle in the Sargasso Sea near Bermuda. Deep-Sea Res. Part I—Oceanogr. Res. Pap. 42 (7), 1215–1237.

Chase, Z., Anderson, R.F., Fleisher, M.Q., Kubik, P.W., 2002. The influence of particle composition and particle flux on scavenging of Th, Pa and Be in the ocean. Earth Planet. Sci. Lett. 204 (1–2), 215–229.

Chase, Z., Anderson, R.F., Fleisher, M.Q., Kubik, P.W., 2003. Scavenging of Th-230 Pa-231 and Be-10 in the Southern Ocean (SW Pacific sector): the importance of particle flux, particle composition and advection. Deep-Sea Res. Part II—Topical Stud. Oceanogr. 50 (3–4), 739–768.

Chiba, H., Masuda, H., Lee, S.Y., Fujioka, K., 2001. Chemistry of hydrothermal fluids at the TAG active mound, MAR 26 degrees N, in 1998. Geophys. Res. Lett. 28 (15), 2919–2922. http://dx.doi.org/10.1029/2000gl012645.

Chung, S.N., Lee, K., Feely, R.A., Sabine, C.L., Millero, F.J., Wanninkhof, R., Bullister, J.L., Key, R.M., Peng, T.H., 2003. Calcium carbonate budget in the Atlantic Ocean based on water column inorganic carbon chemistry. Global Biogeochem. Cycles 17 (4).

Cochran, J.K., Buesseler, K.O., Bacon, M.P., Wang, H.W., Hirschberg, D.J., Ball, L., Andrews, J., Crossin, G., Fleer, A., 2000. Short-lived thorium isotopes (Th-234, Th-228) as indicators of POC export and particle cycling in the Ross Sea, Southern Ocean. Deep-Sea Res. Part II—Topical Stud. Oceanogr. 47 (15–16), 3451–3490.

Cutter, G.A., Andersson, P., Codispoti, L., Croot, P., Francois, F., Lohan, M.C., Obata, H., Rutgers van der Loeff, M., 2010. Sampling and Sample-handling Protocols for GEOTRACES Cruises. ⟨http://www.geotraces.org/libraries/documents/Intercalibration/Cookbook.pdf⟩.

Dammshäuser, A., Wagener, T., Croot, P.L., 2011. Surface water dissolved aluminum and titanium: tracers for specific time scales of dust deposition to the Atlantic? Geophys. Res. Lett. 38 (24), L24601. http://dx.doi.org/10.1029/2011GL049847.

DeMaster, D.J., 1981. The supply and accumulation of silica in the marine environment. Geochim. Cosmochim. Acta 45 (10), 1715–1732. http://dx.doi.org/10.1016/0016-7037(81)90006-5.

Dunne, J.P., Sarmiento, J.L., Gnanadesikan, A., 2007. A synthesis of global particle export from the surface ocean and cycling through the ocean interior and on the seafloor. Global Biogeochem. Cycles 21 (4).

Dymond, J., Collier, R., McManus, J., Honjo, S., Manganini, S., 1997. Can the aluminum and titanium contents of ocean sediments be used to determine the paleoproductivity of the oceans? Paleoceanography 12 (4), 586–593. http://dx.doi.org/10.1029/97pa01135.

Engel, A., Szlosek, J., Abramson, L., Liu, Z., Lee, C., 2009. Investigating the effect of ballasting by $CaCO_3$ in Emiliania huxleyi: I. Formation, settling velocities and physical properties of aggregates. Deep Sea Res. Part II: Topical Stud. Oceanogr. 56 (18), 1396–1407.

François, R., Honjo, S., Krishfield, R., Manganini, S., 2002. Factors controlling the flux of organic carbon to the bathypelagic zone of the ocean. Global Biogeochem. Cycles 16 (4), http://dx.doi.org/10.1029/2001gb001722.

Gardner, W.D., Sullivan, L.G., 1981. Benthic storms: temporal variability in a deep-ocean nepheloid layer. Science 213 (4505), 329–331.

GEOTRACES, 2006. GEOTRACES Science Plan. ⟨http://www.geotraces.org/libraries/documents/Science_plan.pdf⟩.

GEOTRACES, 2010. Sample and Sample-handing Protocols for GEOTRACES Cruises. ⟨http://www.obs-vlfr.fr/GEOTRACES/libraries/documents/Intercalibration/Cookbook.pdf⟩.

German, C.R., Campbell, A.C., Edmond, J.M., 1991. Hydrothermal scavenging at the Mid-Atlantic Ridge: modification of trace element dissolved fluxes. Earth Planet. Sci. Lett. 107 (1), 101–114. http://dx.doi.org/10.1016/0012-821x(91)90047-l.

German, C.R., Von Damm, K.L., 2003. Hydrothermal processes. In: Elderfield, H., Turekian, K.K. (Eds.), Treatise on Geochemistry. Elsevier, pp. 181–222.

Gross, T.F., Williams III, A.J., Nowell, A.R.M., 1988. A deep-sea sediment transport storm. Nature 331, 518–521.

Gundersen, K., Orcutt, K.M., Purdie, D.A., Michaels, A.F., Knap, A.H., 2001. Particulate organic carbon mass distribution at the Bermuda Atlantic Time-series Study (BATS) site. Deep-Sea Res. Part II—Topical Stud. Oceanogr. 48 (8–9), 1697–1718. http://dx.doi.org/10.1016/s0967-0645(00)00156-9.

Hatta, M., Measures, C.I., Roshan, S., Wu, J., Fitzsimmons, J.N., Sedwick, P., Morton, P., 2015. An overview of dissolved Fe and Mn distributions during the 2010-2011 U.S. GEOTRACES North Atlantic Cruises: GEOTRACES GA03. Deep Sea Res. Part II: Topical Stud. Oceanogr. 116, 117–129. http://dx.doi.org/10.1016/j.dsr2.2014.07.005.

Henson, S.A., Sanders, R., Madsen, E., 2012. Global patterns in efficiency of particulate organic carbon export and transfer to the deep ocean. Global Biogeochem. Cycles 26 (1), GB1028. http://dx.doi.org/10.1029/2011gb004099.

Honjo, S., Dymond, J., Collier, R., Manganini, S.J., 1995. Export production of particles to the interior of the equatorial Pacific-Ocean during the 1992 eqpac experiment. Deep-Sea Res. Part II—Topical Stud. Oceanogr. 42 (2–3), 831–870.

Iversen, M.H., Ploug, H., 2010. Ballast minerals and the sinking carbon flux in the ocean: carbon-specific respiration rates and sinking velocity of marine snow aggregates. Biogeosciences 7 (9), 2613–2624. http://dx.doi.org/10.5194/bg-7-2613-2010.

Jeandel, C., Rutgers van der Loeff, M., Lam, P.J., Roy-Barman, M., Sherrell, R.M., Kretschmer, S., German, C.R., Dehairs, F., 2014. What did we learn on the oceanic particle dynamic from the GEOSECS-JGOFS times? Prog. Oceanogr. (in press, accepted on November 21).

Jenkins, W.J., Smethie, W.M., Boyle, E.A., Cutter, G.A., 2015. Water mass analysis for the U.S. GEOTRACES North Atlantic Sections. Deep Sea Res. Part II: Topical Stud. Oceanogr. 116, 6–20. http://dx.doi.org/10.1016/j.dsr2.2014.11.018.

Klaas, C., Archer, D.E., 2002. Association of sinking organic matter with various types of mineral ballast in the deep sea: implications for the rain ratio. Global Biogeochem. Cycles 16 (4), 1116–1129.

Lam, P.J., Bishop, J.K.B., 2007. High biomass low export regimes in the Southern Ocean. Deep Sea Res. Part II: Topical Stud. Oceanogr. 54, 601–638.

Lam, P.J., Bishop, J.K.B., 2008. The continental margin is a key source of iron to the HNLC North Pacific Ocean. Geophys. Res. Lett. 35, L07608. http://dx.doi.org/10.1029/2008GL033294.

Lam, P.J., Bishop, J.K.B., Henning, C.C., Marcus, M.A., Waychunas, G.A., Fung, I.Y., 2006. Wintertime phytoplankton bloom in the subarctic Pacific supported by

continental margin iron. Global Biogeochem. Cycles 20 (1), http://dx.doi.org/10.1029/2005GB002557.
Lam, P.J., Doney, S.C., Bishop, J.K.B., 2011. The dynamic ocean biological pump: insights from a global compilation of particulate organic carbon, $CaCO_3$, and opal concentration profiles from the mesopelagic. Global Biogeochem. Cycles 25 (3), GB3009. http://dx.doi.org/10.1029/2010gb003868.
Lam, P.J., Morris, P.J., Patent pending. In Situ Marine Sample Collection System and Methods. Application No. 13/864,655.
Le Moigne, F.A.C., Sanders, R.J., Villa-Alfageme, M., Martin, A.P., Pabortsava, K., Planquette, H., Morris, P.J., Thomalla, S.J., 2012. On the proportion of ballast versus non-ballast associated carbon export in the surface ocean. Geophys. Res. Lett 39 (15), L15610. http://dx.doi.org/10.1029/2012gl052980.
Lima, I.D., Lam, P.J., Doney, S.C., 2013. Dynamics of particulate organic carbon flux in a global ocean model. Biogeosci. Discuss 10 (9), 14715–14767. http://dx.doi.org/10.5194/bgd-10-14715-2013.
Luo, S.D., Ku, T.L., 2004. On the importance of opal, carbonate, and lithogenic clays in scavenging and fractionating Th-230, Pa-231 and Be-10 in the ocean. Earth Planetary Sci. Lett. 220 (1–2), 201–211.
Macdonald, R., Gobeil, C., 2012. Manganese sources and sinks in the Arctic Ocean with reference to periodic enrichments in basin sediments. Aquat. Geochem. 18 (6), 565–591. http://dx.doi.org/10.1007/s10498-011-9149-9.
Marchal, O., Lam, P.J., 2012. What can paired measurements of Th isotope activity and particle concentration tell us about particle cycling in the ocean? Geochim. Cosmochim. Acta 90 (0), 126–148. http://dx.doi.org/10.1016/j.gca.2012.05.009.
McCave, I.N., 1986. Local and global aspects of the bottom nepheloid layers in the world ocean. Neth. J. Sea Res. 20 (2–3), 167–181. http://dx.doi.org/10.1016/0077-7579(86)90040-2.
McCave, I.N., Hall, I.R., 2002. Turbidity of waters over the Northwest Iberian continental margin. Prog. Oceanogr. 52 (2–4), 299–313. http://dx.doi.org/10.1016/S0079-6611(02)00012-5.
Mortlock, R.A., Froelich, P.N., 1989. A simple method for the rapid-determination of biogenic opal in pelagic marine-sediments. Deep-Sea Res. Part A–Oceanogr. Res. Pap. 36 (9), 1415–1426.
Murnane, R.J., Cochran, J.K., Sarmiento, J.L., 1994. Estimates of particle-cycling and thorium-cycling rates in the Northwest Atlantic-Ocean. J. Geophys. Res.—Oceans 99 (C2), 3373–3392.
Murray, R.W., Leinen, M., 1996. Scavenged excess aluminum and its relationship to bulk titanium in biogenic sediment from the central equatorial Pacific Ocean. Geochim. Cosmochim. Acta 60 (20), 3869–3878.
Nozaki, Y., Yang, H.-S., Yamada, M., 1987. Scavenging of thorium in the Ocean. J. Geophys. Res 92 (C1), 772–778. http://dx.doi.org/10.1029/JC092iC01p00772.
Ohnemus, D.C., Lam, P.J., 2015. Cycling of lithogenic marine particulates in the US GEOTRACES North Atlantic Zonal Transect. Deep Sea Res. Part II: Topical Stud. Oceanogr. 116, 283–302. http://dx.doi.org/10.1016/j.dsr2.2014.11.019.
Ohnemus, D.C., Sherrell, R.M., Lagerstöm, M., Morton, P.L., Twining, B.S., Rauschenberg, S.M., Auro, M.E., Lam, P.J., 2014. Piranha a chemical method for dissolution of polyethersulfone filters and laboratory inter-comparison of marine particulate digests. Limnol. Oceanogr. Methods 12, 530–547. http://dx.doi.org/10.4319/lom.2014.12.530.
Owens, S.A., Pike, S., Buesseler, K.O., 2015. Thorium-234 as a tracer of particle dynamics and upper ocean export in the Atlantic Ocean. Deep- Sea Res. Part II: Top. Stud. Oceangr. 116, 42–59. http://dx.doi.org/10.1016/j.dsr2.2014.11.010.
Parsons, T.R., Maita, Y., Lalli, C.M., 1984. A Manual of Chemical and Biological Methods for Seawater Analysis. Pergamon Press, New York, NY.
Ragueneau, O., Schultes, S., Bidle, K.D., Claquin, P., Moriceau, B., 2006. Si and C interactions in the world ocean: importance of ecological processes and implications for the role of diatoms in the biological pump. Global Biogeochem. Cycles 20, GB4S02. http://dx.doi.org/10.1029/2006GB002688.
Revels, B.N., Ohnemus, D.C., Lam, P.J., Conway, T.M., John, S.G., 2015. The isotopic signature and distribution of particulate iron in the North Atlantic Ocean. Deep Sea Res. Part II: Topical Stud. Oceanogr. 116, 321–331. http://dx.doi.org/10.1016/j.dsr2.2014.12.004.
Riley, J.S., Sanders, R., Marsay, C., Le Moigne, F.A.C., Achterberg, E.P., Poulton, A.J., 2012. The relative contribution of fast and slow sinking particles to ocean carbon export. Global Biogeochem. Cycles 26 (1), GB1026. http://dx.doi.org/10.1029/2011gb004085.
Roy-Barman, M., Jeandel, C., Souhaut, M., Rutgers van der Loeff, M., Voege, I., Leblond, N., Freydier, R., 2005. The influence of particle composition on thorium scavenging in the NE Atlantic ocean (POMME experiment). Earth Planet. Sci. Lett. 240 (3–4), 681–693.
Roy-Barman, M., Lemaître, C., Ayrault, S., Jeandel, C., Souhaut, M., Miquel, J.C., 2009. The influence of particle composition on Thorium scavenging in the Mediterranean Sea. Earth Planet. Sci. Lett. 286 (3–4), 526–534. http://dx.doi.org/10.1016/j.epsl.2009.07.018.
Rudnicki, M.D., Elderfield, H., 1992. Helium, radon and manganese at the tag and snake-pit hydrothermal vent fields, 26-degrees and 23-degrees—N, Mid-Atlantic Ridge. Earth Planet. Sci. Lett. 113 (3), 307–321. http://dx.doi.org/10.1016/0012-821x(92)90136-j.
Rudnicki, M.D., Elderfield, H., 1993. A chemical model of the buoyant and neutrally buoyant plume above the TAG vent field, 26 degrees N, Mid-Atlantic Ridge. Geochim. Cosmochim. Acta 57 (13), 2939–2957. http://dx.doi.org/10.1016/0016-7037(93)90285-5.
Rutgers van der Loeff, M.M., Boudreau, B.P., 1997. The effect of resuspension on chemical exchanges at the sediment–water interface in the deep sea—a modelling and natural radiotracer approach. J. Mar. Syst. 11 (3–4), 305–342. http://dx.doi.org/10.1016/S0924-7963(96)00128-5.
Santos, A.M.P., Kazmin, A.S., Peliz, A., 2005. Decadal changes in the Canary upwelling system as revealed by satellite observations: their impact on productivity. J. Mar. Res. 63, 359–379.
Sarmiento, J.L., Rooth, C.G.H., 1980. A comparison of vertical and isopycnal mixing models in the deep sea based on radon 222 measurements. J. Geophys. Res.: Oceans 85 (C3), 1515–1518. http://dx.doi.org/10.1029/JC085iC03p01515.
Taylor, S.R., McLennan, S.M., 1995. The geochemical evolution of the continental-crust. Rev. Geophys. 33 (2), 241–265.
Ternon, E., Guieu, C., Loye-Pilot, M.D., Leblond, N., Bosc, E., Gasser, B., Miquel, J.C., Martin, J., 2010. The impact of Saharan dust on the particulate export in the water column of the North Western Mediterranean Sea. Biogeosciences 7 (3), 809–826. http://dx.doi.org/10.5194/bg-7-809-2010.
Thomalla, S.J., Poulton, A.J., Sanders, R., Turnewitsch, R., Holligan, P.M., Lucas, M.I., 2008. Variable export fluxes and efficiencies for calcite, opal, and organic carbon in the Atlantic Ocean: a ballast effect in action? Global Biogeochem. Cycles 22 (1), GB1010.
Thorpe, S.A., 1972. A sediment cloud below the Mediterranean Outflow. Nature 239, 326–327.
Toner, B.M., Fakra, S.C., Manganini, S.J., Santelli, C.M., Marcus, M.A., Moffett, J., Rouxel, O., German, C.R., Edwards, K.J., 2009. Preservation of iron(II) by carbon-rich matrices in a hydrothermal plume. Nat. Geosci. 2 (3), 197–201. http://dx.doi.org/10.1038/Ngeo433.
Trefry, J.H., Trocine, R.P., Klinkhammer, G.P., Rona, P.A., 1985. Iron and copper enrichment of suspended particles in dispersed hydrothermal plumes along the Mid-Atlantic Ridge. Geophys. Res. Lett. 12, 506–509.
Trocine, R.P., Trefry, J.H., 1988. Distribution and chemistry of suspended particles from an active hydrothermal vent site on the Mid-Atlantic Ridge at 26°N. Earth Planet. Sci. Lett. 88, 1–15.
Wakeham, S.G., Canuel, E.A., 1988. Organic geochemistry of particulate matter in the eastern tropical North Pacific Ocean: implications for particle dynamics. J. Mar. Res. 46 (1), 183–213.
Wilson, J.D., Barker, S., Ridgwell, A., 2012. Assessment of the spatial variability in particulate organic matter and mineral sinking fluxes in the ocean interior: implications for the ballast hypothesis. Global Biogeochem. Cycles 26 (4), GB4011. http://dx.doi.org/10.1029/2012gb004398.